The Stellar Mass Spectrum of the Open Cluster NGC 3293

Robert W. Slawson[1], Zoran Ninkov, and Elliott P. Horch[12]

Center for Imaging Science, Rochester Institute of Technology

54 Lomb Memorial Dr., Rochester, NY 14623-5604

electronic mail: [slawson,ninkov,horch]@cis.rit.edu

Received _____; accepted _____

[1]Guest investigators at the University of Toronto Southern Observatory, Las Campanas, Chile

[2]Present address: Department of Physics, Southern Connecticut State University, 501 Crescent Street, New Haven, CT 06515

ABSTRACT

We have obtained and analyzed *UBVRI* CCD frames of the young, 4–10 Myr, open cluster NGC 3293 and the surrounding field in order to study its stellar content and determine the cluster's IMF. We found significantly fewer lower mass stars, $M \leq 2.5 M_{\odot}$, than expected. This is particularly so if a single age for the cluster of 4.6 Myr is adopted as derived from fitting evolutionary models to the upper main sequence. Some intermediate-mass stars near the main sequence in the HR diagram imply an age for the cluster of about 10 Myr. When compared with the Scalo (1998) IMF scaled to the cluster IMF in the intermediate mass range, $2.5 \leq M/M_{\odot} \leq 8.0$ where there is good agreement, the high mass stars have a distinctly flatter IMF, indicating an over abundance of these stars, and there is a sharp turnover in the distribution at lower masses. The radial density distribution of cluster stars in the massive and intermediate mass regimes indicate that these stars are more concentrated to the cluster core whereas the lower-mass stars show little concentration. We suggest that this is evidence supporting the formation of massive stars through accretion and/or coagulation processes in denser cluster cores at the expense of the lower mass proto-stars.

Subject headings: open clusters and associations: individual (NGC 3292) — stars: luminosity function, mass function

1. Introduction

The young open cluster NGC 3293 (C1033-579) ($\ell = 285\overset{\circ}{.}86, b = 0\overset{\circ}{.}07$) is associated with the Car OB1 complex in the η Car region of the Galaxy (Ruprecht 1966; Turner, et al. 1980). Photographed by Gould (Hazen 1991) during his 1872–82 expedition to Córdoba Argentina, NGC 3293, as for most of the southern OB clusters, has not received a great deal of attention (although more than most). This cluster is not completely removed from the rich complex of ionized gas and dust in the vicinity of the Carina Nebula (NGC 3372). At a distance of about 2.5 kpc, NGC 3293 is in a group of young clusters that also contains Tr 14, Tr 15, Tr 16, Cr 228, NGC 3324, and IC 2581 (Turner, et al. 1980; Feinstein & Marraco 1980).

Feast (1958) obtained photographic radial velocities and determined spectral types for the brightest B stars in the cluster and in the surrounding region. Feinstein & Marraco (1980) and Turner, et al. (1980) obtained $UBV(RI)$ photoelectric magnitudes for many of the potential B-type stars associated with the cluster and determined the cluster's reddening and distance. Shobbrook (1980, 1983) and Balona (1994) have observed the cluster in the Strömgren $uvby\beta$ system photoelectrically and with a CCD respectively. Balona (1994) noted that there are an unusually large number of β Cep stars, eleven, in the cluster.

Herbst & Miller (1982) use star counts based on photographic photometry to derive the IMF for the cluster. It is this study that first showed that the cluster's IMF differs from the standard form (Scalo 1986). Their Luminosity Function for the cluster has a marked deficit of M_V=1–2 stars resulting in an IMF that turns over at 3–4 $M_\odot$ and declines for less massive stars. In other words, the number of low mass stars is deficient when compared to that expected given the number of high mass cluster members. Evidently, most of the mass that was turned into stars in this cluster preferentially formed into higher mass stars. In addition, they found evidence in their data for an age spread among the main-sequence

cluster stars of ~ 20 Myr with the least massive stars being the oldest.

In his review of the Initial Mass Function (IMF), Scalo (1986, 1998) found that the only open cluster showing convincing evidence for a turnover in its IMF at an intermediate mass is NGC 3293. One criticism of studies purporting turnovers in the IMF of clusters at intermediate and lower masses is that the observed turnover is typically too close to the observational completeness limit. This leads to the suspicion that some, or all, of the discrepancy is an observational artifact. Forbes (1996) points out, in his study of NGC 6531, that a gap in a cluster color-magnitude diagram below the point where stars are just reaching the zero-age main sequence is expected from evolutionary considerations. In this phase of their life, pre-main-sequence stars are rapidly evolving blueward resulting in a thin population in this region of the diagram. A cluster membership survey needs to reach sufficiently redward and fainter in order not to exclude pre-main-sequence stars massive enough to, in time, populate this part of the main-sequence.

With the advances in solid-state imaging technology the time seemed ripe for CCD photometry of this cluster to further investigate the turnover of its IMF. CCD's have a considerable advantage in detection efficiency over photographic plates throughout the optical spectrum particularly at red wavelengths. The point spread function (PSF) fitting technique enables better photometry in the crowded field of the cluster's core. As well, an estimate of the fractions of fainter stars missed due to crowding effects and the PSF wings of bright stars are available from the recovery of artificial stars randomly added to the digital images. This leads to more accurately determined completeness limits and corrections for undercounts of potential faint, low-mass, cluster members.

We have acquired *UBVRI* images of NGC 3293 covering the field studied by Herbst & Miller (1982) and extending outward to larger radial distances from the cluster center, in some directions up to twice the cluster's coronal radius. Our limiting magnitude from PSF

fitting photometry of $V = 19\overset{m}{.}2$ is also $\sim 2\overset{m}{.}5$ magnitudes fainter than what they measured on their plate material. Figure 1 is a mosaic of our V frames and shows the field covered by this study. The circle denotes the approximate coronal radius of the cluster and the area covered in this study within and outside this boundary is nearly the same. Our primary goal in this work was to extend the search for potential intermediate and low-mass cluster stars to better determine the IMF of this interesting cluster.

Towards this end, the next section, §2, details the observational data acquired and its calibration. §3 describes our data analysis and includes, in §3.1, a multicolor approach to dereddening that we have not seen previously described. We discuss our completeness limits in §3.4 which are, as always, very important when examining the faint end of a LF based on magnitude limited data. In §4 we determine the initial mass function for the cluster and examine the distribution of stars in the cluster, and §5 attempts to place the IMF of NGC 3293 within the context of current ideas about the formation of massive stars in cluster environments.

2. Observational Material

2.1. Data Acquisition

During 2 observing runs in March 1996 (RWS) and February 1997 (EPH) CCD images were acquired through Bessell *UBVRI* filters of the central and peripheral regions of the open cluster NGC 3293. Our own Photometrics CH250 camera containing a 2K×2K by 9μ square pixel, Lumogen-coated Kodak KAF-4200 CCD was used in conjunction with the tip-tilt guiding camera at the University of Toronto Southern Observatory 61 cm telescope on Las Campanas. (Alas, operation of the UTSO telescope ceased Dec. 1997.) At the cassegrain focus, the image scale is $0\overset{''}{.}19$/pixel and the typical PSF is 5–8 pixels FWHM.

A brief journal of the observations is given in Table 1.

The field of view of these CCD frames are $7'$ square and frames were obtained centered on the cluster and in several offset, overlapping fields. Figure 1 is a mosaic of the longer exposure V frames acquired of the cluster and surrounding field. The field is sampled out to $12'$ from the cluster center. The camera was rotated $15°$ between observing runs allowing the recovery of a few fainter stars that would otherwise be lost from CCD blooming and diffraction effects near the bright stars.

Flatfield frames for all filters were acquired during twilight whenever possible. Bias frames were acquired at intervals throughout the night during the 1996 observing run but a bias strip was added to each CCD data frame in 1997. *UBVRI* standard stars were observed in several of Landolt's (1992) CCD fields at several times during photometric nights covering the same range in airmass as the data frames. On a few nights, some E-region standard stars (Graham 1982) were also observed.

2.2. Reduction

Basic reduction of the raw CCD frames and subsequent PSF fitting photometry was largely carried out with the `ccdproc` and `daophot` tasks within IRAF.[1] The frames were trimmed and bias subtracted. For the 1996 frames, the bias was removed by subtracting the mean bias level from each pixel as determined by averaging the bias frames acquired periodically through the night. In 1997, the bias level of each frame was determined from an overscan strip (which is a superior method as little or no structure is apparent in an

[1]IRAF is distributed by the National Optical Astronomy Observatories, which are operated by the Association of Universities for Research in Astronomy, Inc., under cooperative agreement with the National Science Foundation.

average of 100+ bias frames). About 50 pixels in one column near the edge of the CCD were replaced with interpolated values from nearest neighbors.

Experimentation showed that subtraction of dark frames tended to increase the background noise as did any of the cosmic ray cleaning algorithms. Since the PSF's are typically 5–8 pixels FWHM (1–1.″4), the statistical rejection of outlying pixels during PSF fitting proved to be the best method of removing both hot-pixels and cosmic ray events from the measurements.

After examining the flatfield frames for individual nights it was decided to combine together all the frames in each filter within each year. This yielded two sets of flatfield images applicable to all the frames. It is our experience that the accuracy of CCD photometry is usually limited by the accuracy of the flatfield correction; therefore the highest S/N flatfield frame for each filter is desired. All the data and standard star frames were divided by the appropriate, normalized flatfield frames.

Standard stars were measured with the IRAF IRAF task `apphot` task using a common aperture of 11.″4 diameter on the sky. Stars on frames of the cluster field were measured with PSF fitting techniques as implemented in the IRAF IRAF task `daophot` task. Care was taken to tune the algorithm parameters to the PSF and background noise of each individual frame. This included using up to 40 bright, isolated stars for modeling the PSF in each frame. Frame-by-frame aperture corrections were computed using the PSF modeling stars with any neighboring stars subtracted and the IRAF task `mkapfile`. These corrections were then applied to the PSF photometry as a frame-by-frame zero-point correction to place the PSF photometry on the same system as the standard stars.

All the frames were registered to a common pixel coordinate system using the overlapping portions of the frames. This included small corrections for field rotation and scale changes (due to focus changes) as needed to ensure accurate collation of the data for

each star with a tolerance of about 0.″7. This was easily checked by examining a mosaic image of the frames after applying to each frame its registration transformation. Thus overlapping star images were separated if the image centers were separated by more than $\sim 1/2$ FWHM of the PSF corresponding to $\sim 2\,000$ AU at the cluster distance.

2.3. Calibration

Coefficients for the following transformation equations were computed by least-squares fitting to the standard star data:

$$u - U = a_0 + a_1 X_i + a_2(U - B) + a_3 X_i (U - B),$$

$$b - B = c_0 + c_1 X_i + c_2(B - V) + c_3 X_i (B - V),$$

$$v - V = d_0 + d_1 X_i + d_2(V - R) + d_3 X_i (V - R),$$

$$r - R = e_0 + e_1 X_i + e_2(V - R) + e_3 X_i (V - R),$$

$$i - I = f_0 + f_1 X_i + f_2(R - I) + f_3 X_i (R - I).$$

The coefficients k_0, k_2, k_3, the zero-point and color terms, apply to all the frames in that particular filter on photometric nights over the entire observations. These coefficients are assumed to apply to all the data from all nights over both years as the complete instrument (primary mirror to CCD) was identical for both observing runs. k_1, the primary extinction coefficient, was determined individually for each photometric night. X_i is the airmass at which frame i was obtained. On non-photometric nights, the coefficients k_2, k_3 were assumed still valid (thin clouds are neutral grey) and, for each frame, the term $(k_0 + k_1 X_i)$ was determined as a zero-point correction by averaging the differences between the photometry of stars in the frame and the corresponding mean transformed values from the photometric nights. Table 2 lists the coefficients where the k_1 are the means of the nightly extinction

term. Typical residuals from this procedure were $0\overset{m}{.}02$–03. Mean values and standard deviations ($n > 1$) were computed for all stars with transformable data which required measurements in at least the filters V and R. Figure 2 shows the estimated photometric uncertainties for all the stars for which standardized magnitudes were computed.

2.3.1. Comparison with Previous Data

The largest existing set of photoelectric photometry for NGC 3293 is that of Turner, et al. (1980). In Figure 3 we compare their UBV measures with our calibrated photometry for the 92 stars in common. The only concern is with the U values where a constant, systematic difference of $0\overset{m}{.}036 \pm 0\overset{m}{.}05$ (after removing outliers) is noted. Turner, et al. (1980) also note that they had problems with their $U-B$ calibration for some of their data, resorting to a correction of $0\overset{m}{.}03$ for those stars affected. There are known systematic differences between the northern (which includes the equatorial standards used here) and southern (used by Turner, et al. (1980)) photoelectric systems that could account for much of the difference found here.

3. Data Analysis

3.1. Dereddening

To deredden the data, we strove to use as much of the information available as possible, preferably colors from all 5 filters, and developed a procedure that is free of the degeneracy (multiple solutions) encountered for B9 through F stars when dereddening is attempted using the $(B-V), (U-B)$ diagram.

In the 3-color space $(B-V, U-B, R-I)$, the intrinsic colors of main-sequence stars is

a curve through the space. The common $(B-V, U-B)$ diagram is the just the projection of this 3-dimensional main-sequence color relation onto the $(B-V, U-B)$ plane which, in this color space, is perpendicular to the $(R-I)$ axis. To make use of the $(R-I)$ color, construct the reddening vector $\mathbf{A}$ and project the intrinsic relation onto a plane perpendicular to $\mathbf{A}$. Finding the reddening free colors of a star involves projecting the point in 3-color space corresponding to the stars observed colors onto the plane perpendicular to $\mathbf{A}$ and choosing the "closest" point on the projected intrinsic color curve.

The reddening vector $\mathbf{A} = 1/A_V[A_B - A_V, A_U - A_B, A_R - A_I]$ where the $A(\lambda)/A_V$ values are available from general reddening law tabulations (Rieke & Lebofsky 1985) or fitted formulae (Cardelli, Clayton, & Mathis 1989). For simplicity, we ignore any possible curvature terms in the reddening law: neither Rieke & Lebofsky (1985) nor Cardelli, Clayton, & Mathis (1989) discuss a curvature term and the *UBV* study by Turner (1978) of the photometric reddening in a number of Galactic fields prefers a zero (or small) curvature term. Then the projection of the point P corresponding to the observed colors onto a plane perpendicular to $\mathbf{A}$ is $P' = P - [\mathbf{A} \cdot P]\mathbf{A}$ by straight forward linear algebra. (Here $\mathbf{A}$ is normalized, $||\mathbf{A}|| = 1$).

Figure 4 shows the reddening free colors for stars with surface gravities of $\log g = 4.0, 4.5$ from the synthetic *UBVRI* photometry of Bessell, Castelli, & Plez (1998) projected onto the plane perpendicular to the reddening vector corresponding to the Cardelli, Clayton, & Mathis (1989) reddening law with $R_V = 3.1$. The reddening vector is pointing at the observer. $(B-V)_0$ values along these curves are indicated for reference. Also shown is the projected effect of $\pm 0\overset{\mathrm{m}}{.}03$ uncertainties in each of the *UBVRI* passbands.

In general, stars in this dereddened plane will not fall on the appropriate intrinsic relation due to photometric errors. To find the "closest" point on the intrinsic relation, we projected onto the plane an error ellipse for each star computed from the estimated

uncertainties in its photometry. We then scaled the ellipse to the smallest size that osculates the intrinsic curve at one point and adopted the corresponding colors as the reddening free colors of that particular star. The total extinction, A_V, of the star is the distance between the two planes perpendicular to **A** one containing this point and the other the star's observed colors. The color excess is $E_{B-V} = A_V/R_V$ where the value of $R_V = 3.1$ for the ratio of total to selective absorption, as determined in and around NGC 3293 by Turner, et al. (1980), was adopted throughout.

A similar approach was employed for dereddening stars without useable measures in U but otherwise complete $BVRI$ data. In this case, the $(B-V, V-I, R-I)$ colors were projected onto the plane perpendicular to **A** again with the synthetic, intrinsic colors of Bessell, Castelli, & Plez (1998) for main-sequence stars ($\log g = 4.0, 4.5$). The intrinsic color sequence (loci of points), however, occupies a smaller part of this plane than when all 5 filters are available which leads to a greater sensitivity to uncertainties and consequently larger errors in the derived color excesses. This arises because the reddening vector is more nearly parallel to the intrinsic sequence, a situation that is clear in 2-color diagrams constructed from the same colors or other combinations of these 4 magnitudes. Munari & Carraro (1996) have examined this problem. For this reason, we preferred the solution from 5-color photometry to that from only 4 colors whenever available.

As a check on our procedure, we have compared the color excesses determined by Turner, et al. (1980) with those determined here for all the stars in common and display the result as Figure 5. Those stars that Turner, et al. (1980) derived their color excess from MK spectral types are marked with filled circles and the remaining, based on UBV photometry alone, with open circles. The two outliers, stars 78 & 111, have colors that place them in the region of the 2-color diagram where dereddening is most difficult. Excluding these, the mean difference and the dispersion are $-0\overset{\mathrm{m}}{.}011 \pm 0\overset{\mathrm{m}}{.}045$.

With the additional information of MK spectral types, Turner, et al. (1980) examined the reddening law in the cluster and surrounding region. While essentially a normal law, their reddening slopes are slightly different than those of Cardelli, Clayton, & Mathis (1989)'s general law. For $R_V = 3.1$, the CCM89 law yields, $E_{U-B}/E_{B-V} = 0.763$, $E_{V-R}/E_{B-V} = 0.771$, and $E_{V-I}/E_{B-V} = 1.62$ whereas TGHH determined 0.74, 0.82, and 1.72 for the same ratios. In Figure 6a we show our *UBVRI* data in the dereddened plane corresponding to the CCM89 law. Figure 6b shows the same data projected onto the dereddened plane consistent with TGHH's reddening law. There are small differences in the plots and in Fig. 6c we show the differences in E_{B-V} derived from the two laws. Most of the color excess differences are small, $\leq 0\overset{\mathrm{m}}{.}01$, less than the scatter between our color excesses and those of Turner, et al. (1980) shown in Figure 5. The few large negative differences result when a star is closer to a different section of the adopted main-sequence according to one reddening law but not the other. Most of the affected stars are between $-0.10 < B - V < 0.30$ (see Fig.4). This illustrates that the ambiguities that arise in this region of the 2-color diagram return in our 3-color cube as the photometric uncertainties become larger.

In both Figure 6a and 6b, the OB-stars, in the lower left of the diagram, appear to lie slightly rightward of the adopted synthetic main sequence. In fact, a systematic shift of -0.02 in our B magnitudes would place both the $\log g = 4.0$ and $\log g = 4.5$ curves within the cloud of points corresponding to the upper main-sequence of the cluster. When this is done, the red stars are no longer coincident with the main sequence in the upper right part of the diagram. Shifts of the same magnitude in either V, R, or I will have nearly the same effect as indicated in Figure 4. Serious errors in the photometry are not tolerated by this dereddening technique. There is also the implicit assumption that the observational data has been standardized to the identical photometric system employed for the synthetic photometry defining the intrinsic color sequence. That is, the complete

instrumental response functions are the same, not just the filter passbands. Bessell, Castelli, & Plez (1998) Appendix E has an excellent discussion of the potential problems that lead to systematic discrepancies between model and standard system colors.

Attempting to employ an incorrect reddening law yields an obviously inconsistent result as shown in Figure 6d). For this diagram, we adopted the Cardelli, Clayton, & Mathis (1989) reddening law when $R_V = 5.0$. Such a ratio of selective-to-total absorption may be appropriate in molecular clouds where the dust grains may grow to larger sizes than typical in the general ISM. For this value of R_V, the slopes required by the CCM89 law are $E_{U-B}/E_{B-V} = 0.674$ and $E_{R-I}/E_{B-V} = 1.208$. Clearly, this anomalous reddening law does not apply to the cluster; the observed colors for the OB-stars dereddened with this law are inconsistent with the intrinsic colors of *any* stars. Two B-stars in the cluster that TGHH suggest suffer from anomalous extinction (#s 2 & 19) are identified in the figure. Based solely on our *UBVRI* photometry the observed colors of both these stars are consistent with a normal reddening law.

Further investigation into the propagation of photometric uncertainties to other derived quantities is pursued in the next section.

3.2. Astrophysical Values

Bessell, Castelli, & Plez (1998) have also listed the astrophysical quantities $\log T_e$ and $M_{\rm bol}$ derived from the convolution of their filter passbands with recent stellar atmosphere models.

The synthetic photometry of Bessell, Castelli, & Plez (1998) provides a direct relation between a star's broad-band colors and its effective temperature and bolometric correction. As the final step in the dereddening procedure describe in §3.1, both $\log T_e$ and bolometric

corrections were interpolated from the tables for each star. Although there are regions on the projected dereddening plane where the intrinsic color relation for stars at different $\log g$s are not degenerate, the separation is almost always less than the observational uncertainty in our data. Therefore, when deriving $\log T_e$ and $M_{\rm bol}$ for individual stars, a value for $\log = 4.0 - 4.5$ was assumed.

The accuracy of the observations affects the derived values of $\log T_e$ and the bolometric correction and, ultimately, the mass determined for each star. To investigate the effect that photometric uncertainties have on the derived E_{B-V}, $\log T_e$, and bolometric corrections, we dereddened synthetic observations to which noise was added. Noise free *UBVRI* magnitudes appropriate for stars with colors in the range $[-0.315 \leq (B-V)_0 \leq 1.4]$ were generated from the Bessell, Castelli, & Plez (1998) calibrations. These were reddened to $A_v = 1\overset{\rm m}{.}5$ using the mean CCM89 reddening law ($R_V = 3.1$) and random Gaussian deviates with dispersions of $0\overset{\rm m}{.}01$ or $0\overset{\rm m}{.}02$ were added to all 5 magnitudes. One thousand observations at each $(B-V)_0$ and precision level were dereddened as described in §3.1 and the resulting dispersion in E_{B-V}, $\log T_e$, and bolometric correction determined. The results are summarized in Fig. 7.

As expected, larger measurement errors lead to larger uncertainties in the derived quantities and that the precision varies throughout the range in $(B-V)_0$. Similar to the usual 2-color diagram, there are ranges in the 3-dimensional color space where the reddening vector is closer to the tangent of the intrinsic color relation (although not obvious in projection) and in these regions the sensitivity to photometric errors increases. This effect is evident in Fig. 6b ($\sigma_{m_i} = 0.02$) in the range $0.2 \leq (B-V)_0 \leq 0.5$ which corresponds to the range in the $U-B, B-V$ diagram where the reddening line does become tangent to the main-sequence. The degeneracy in the *UBVRI* system for the hottest stars is also evidenced by the rapid increase in the uncertainty of the bolometric correction for $(B-V)_0 \leq -0.25$. There is another region around $B-V = 1.1$ where some degeneracy is present, in Fig. 4,

this is the sharp bend near the point $(0.2, 0.5)$.

3.3. Data Table

The complete table of our standardized *UBVRI* observations of stars in and around the cluster NGC 3293 is available from the authors. Only a sample is shown here as Table 3. The table contains the mean measured V, B, U, R, and I magnitudes, their uncertainty σ in mmag, and the number of frames contributing to the mean. We have estimated the σ's as follows: For each individual measurement, we use the harmonic sum of the σ from the PSF photometry with the σ from the aperture correction. Although we believe our noise model for the photometry is reasonable, we apply a floor to these σ's and require that they be at least $0\overset{\mathrm{m}}{.}008$. When only a single measure is available, this is the value in the table. Otherwise, the quoted σ is the greater of the standard deviation of the transformed magnitudes about their mean and, the uncertainty of the mean multiplied by the square root of the number of measures. In this sense, tabulated σ represents the uncertainty of a single observation. In the complete table, available from the authors, a magnitude of 0.000 implies not measured.

We have identified the stars by their equatorial coordinates in the GSC system (epoch J2000.0). 136 GSC stars were matched with stars in the observed field, a transformation from the pixel to equatorial system computed, and then equatorial coordinates were computed for all the stars. The rms radial error between the computed and cataloged positions for the identified GSC stars is 0.77 pixels or $0\overset{''}{.}15$. The GSC stars are identified in Table 3.

Also cross referenced are numbered stars from Feast (1958), Turner, et al. (1980), and Herbst & Miller (1982). We note the following duplications: #43 in Feast is the same as

#293 in Herbst & Miller; stars 55 and 56 in Turner, et al are the same as 482 and 483 in Herbst & Miller; and that Feinstein & Marraco (1980) stars 52, 53, 54, 55, 56, 57, and 58 are the same as 133, 131, 129, 132, 65, 75, and 87 respectively in the numbering system of Turner, et al. Balona (1994) also extended the numbering system of Turner et al. in his $uvby\beta$ study of NGC 3293 but, unfortunately, his designations were different than those of Herbst & Miller and we have not cross-referenced them here.

3.4. Completeness Limits

As is evident in Fig. 1, the cluster core is dominated by a number of very bright stars. On deep frames the PSF's of these stars have large saturated cores and extensive wings. Faint stars in this region are either lost in the saturated cores or must be detected against the higher background of these bright star aureoles. Thus, the magnitude limits for detecting faint stars and the undercount correction estimates will be functions of both the stellar magnitude and the distance of the stars from the brightest stars in the cluster center.

To investigate the detection limit at faint magnitudes, we added artificial stars with the IRAF task `addstar` to two deep V frames acquired on different nights. One frame has the cluster core slightly off-center and the other has the center in one corner of the frame. Numerous experiments were performed each consisting of 100 artificial stars within a $0\overset{m}{.}5$ interval randomly scattered throughout the image. PSF photometry was then performed on each of these frames using the same IRAF parameters employed on the originals and the detected fraction of artificial stars determined in annular sections of $0'.5$ width centered on the cluster. A weighted average of the recovery fraction at each radius and magnitude interval was computed and these are summarized by the family of curves in Figure 8.

Each curve in Figure 8 represents the fraction of stars recovered within the half

magnitude interval indicated as a function of distance from the cluster center. ¿From this diagram we adopt an 80% completeness limit of $V = 19\overset{m}{.}2$ (transforming instrumental to observed magnitudes assuming $B-V = 1.0$) for stars $r > 4'$ from the cluster center. Towards the center of the cluster the 80% completeness limit is $V = 17$. Note that, even at $V = 14$ magnitude, a significant number of stars are *not* recovered in the central region. Artificial star recovery experiments on U and I frames showed that the instrumental magnitude completeness limits are similar and, therefore the observed magnitude limits can be computed through the photometric transformation equations. Assuming $B-V = 1.0$ the observed magnitude limits for the other filters are: $U = 16.9$, $B = 18.6$, $R = 19.1$, and $I = 19.0$.

Below, we show in an H-R diagram (Figure 10) where these magnitude limits are important. We also apply an area weighted correction (Table 4) for the expected undercount when constructing the clusters IMF(§4.3).

3.5. Radial Star Counts

We adopted the position of the cluster's center as determined by Turner, et al. (1980) from star counts, and placed annuli around the cluster in $0'.5$ steps in radius. As can be seen in Fig. 1, beyond about $4'$ the annuli are only partially filled by our images. Areas for these annuli were determined by Monte Carlo integration. The area of sky sampled by the images inside the adopted cluster boundary, $5'.5$, is very nearly the same as sampled outside the boundary despite the radii extending to $\sim 13'$.

To estimate the extent of the cluster, we counted stars from the dereddened data set in annular rings concentric with the cluster's center. The result is shown in Figure 9(a) for two equal magnitude ranges, $6 \leq V_0 \leq 12$ and $12 \leq V_0 \leq 18$. The ring widths are $1'$ and the

area covered is this bounded region in Figure 1. Undercount corrections were not applied to the inner region as the intent is to determine the outer radius of the cluster where these corrections are small. Note that beyond a radius of $\sim 4\farcm5$ the annuli are only partially complete and at $9'$ only a small sector is sampled.

In both magnitude ranges the central core is well defined as is a minimum in the star counts at $5\farcm5$. We attribute the increase in the stellar surface density observed beyond $8'$ to a group of stars in the vicinity of HD 91824 (star #1, the brightest star $9'$ NW of the cluster in Figure 1). This O7 V star is not a probable member of the cluster (Turner, et al. 1980; Feinstein & Marraco 1980) but is likely a member of the Carina OB1 association of which NGC 3293 is itself a probable component. As there are a number of brighter stars associated with HD 91824, as seen in the lower plot in fig. 9a, it is probably not an isolated run-away from the cluster.

We also counted stars in a $30' \times 30'$ Digital Sky Survey[2] R-band image centered on NGC 3293. Stellar objects were detected with the IRAF `daofind` task but no further calibration attempted. Except for the inner $2'$core of the cluster where crowding and severe saturation of the bright star images in the original photographic plate render indentifying stars difficult, all the detected stellar objects were counted in $0\farcm5$ concentric rings out to a radius of $15'$from the cluster center. These star counts are shown in Figure 9b where the larger sampled area leads to a better determined mean background stellar surface density than star counts from our data. The cluster radial profile appears truncated at a radius

[2]The Digitized Sky Survey was produced at the Space Telescope Science Institute under U.S. Government grant NAG W-2166. The images of these surveys are based on photographic data obtained using the Oschin Schmidt Telescope on Palomar Mountain and the UK Schmidt Telescope The plates were processed into the present compressed digital form with the permission of these institutions.

of 5.′5, although the effect may be a result of the bin choices, and justifies considering this radius as the cluster's outer boundary.

4. The Mass Function

4.1. Theoretical H-R Diagram

Massey et al. (1995) show quite convincingly that masses for the bluest stars, $(B-V)_0 \leq -0.27$, deduced from their positions in an HRD based solely on broad-band photometry are subject to rather large errors. This is a consequence of the degeneracy of the *UBV* system that occurs when the bulk of the spectral energy distribution is in the UV and the optical passbands are only sampling the Rayleigh-Jeans slope. In this regime, the color indices are insensitive to the effective temperature of a star which leads to a poor estimate of its bolometric correction. Even small uncertainties in the photometry may result in significant uncertainties in the placement of a star in the HRD and, in particular, its position relative to theoretical mass tracks from which a mass estimate for the star is determined.

MK spectral types for 25 of the brightest stars in the cluster were determined by Turner, et al. (1980) as part of their study of NGC 3293. Following Massey et al. (1995), we use the effective temperature and bolometric correction calibrations of Humphreys & McElroy (1984) for all but the O7 V star (#1) where Chlebowski & Garmany (1991)'s calibration is used to assign T_e and B.C.'s to those stars with known spectral types. Masses were then determined for these stars by interpolating between Schaller, et al. (1992) evolutionary models.

For all the stars with only *UBVRI* or *BVRI* photometry that could be dereddened using the 3-dimensional color cube (§3.1), effective temperatures and bolometric corrections

were assigned assuming the stars have main-sequence like surface gravities (§3.2). These are available from the synthetic photometry of Bessell, Castelli, & Plez (1998) used for dereddening as they directly link the Bessell *UBVRI* passbands to modern stellar atmosphere models. We also limited the dereddening to stars with $\sigma \leq 0\overset{\mathrm{m}}{.}07$ (m.e.) in all colors since stars with larger uncertainties often yielded clearly spurious results. We point out that virtually all these stars are fainter than the 80% completeness limits shown in Figure 2. Fainter stars for which U and B measures could not be determined from our data, are examined later in §4.2.

In Figure 10 we construct a $\log T_e, m_{\rm bol}$ diagram which includes all the stars in the dereddened dataset. The area covered by the CCD frames is about twice the area of the cluster, within its coronal boundary of $5\farcm5$ radius (Fig. 1,9), so a significant number of field stars contaminates the diagram. Geneva evolutionary models for both post-ZAMS (Schaller, et al. 1992), $M/M_\odot \geq 2.5$, and pre-main-sequence (Bernasconi 1996), $M/M_\odot \leq 2.5$, are overplotted.

Examining the lower main sequence in Figure 11, $4.0 \lesssim \log T_e \lesssim 4.15$, where evolutionary effects are small, one sees a distinct main sequence that is very consistent with the cluster distance modulus, $m - M = 11\overset{\mathrm{m}}{.}99 \pm 0\overset{\mathrm{m}}{.}13$, determined previously by Turner, et al. (1980). In this diagram, the sample has been restricted to the stars within a $5\farcm5$ radius of the cluster center and having color excesses in the range $0.20 \leq E_{B-V} \leq 0.43$. (This is the range in reddenings for cluster stars determined by Turner, et al. from MK spectral type classifications). The main sequence is the 10 Myr isochrone for the Geneva evolutionary models (Schaller, et al. 1992) which differs from their zero-age models only slightly at the hotter effective temperatures. Based on the good agreement, we adopt $m - M = 11.99$ as the distance modulus for the cluster.

To help delineate a region in this diagram that contains plausible cluster members,

all the stars considered cluster members in Turner, et al. (1980) were identified and the selection region was required to include all these stars. The greyed region in Figure 10 is the band in which all their stars are found (including two bright stars for which our CCD data were saturated). The limits above and below the main sequence are $-1\overset{m}{.}00$ and $+0\overset{m}{.}25$ for the unevolved intermediate mass stars. A substantial broadening of this band was required to encompass all the more massive early B stars that have evolved away from the ZAMS. This may reflect a range in ages for these stars although binarity and rapid rotation are also likely contributors. The red supergiant, star #21, is consistent with the age but the two most luminous B stars imply a younger age. (Perhaps they are blue stragglers resulting from the merger of binary systems).

Since the photo-electric photometry of Turner, et al. (1980) only covers the upper and mid portions of the main sequence, a band of the same width is extended along an isochrone of 10 Myr in the Geneva pre-main-sequence models of Bernasconi (1996). There is an obvious gap around $2M_{\odot}$ with a continuation of the main sequence near $1.7M_{\odot}$. Most the stars in this grouping fall within selection band.

Evolutionary (mass) models from the Geneva group, (Schaller, et al. 1992) are overlaid on the H-R diagram. For stars selected as pre–main-sequence stars, the models of Bernasconi (1996) were used. Using these, masses for all the stars, including those placed in the HRD based on spectral type calibrations, were assigned by interpolation between the mass models.

In an attempt to avoid misrepresenting the pre-main-sequence component of the IMF, in what follows, we adopt based on the radial star counts discussed elsewhere (§3.5), that all HRD selected stars that lie outside the cluster boundary are field stars. Their surface density is then subtracted from the surface density of similarly selected stars within the cluster boundary yielding an estimate of the number of true cluster members. In this

way, the derived IMF of the cluster should be immune to background and interloping star contamination both of which become more important at fainter magnitudes and redder colors.

4.2. $(V, V-I)$ Diagrams

About half the calibrated dataset consists of stars with only V,R, and I observations. As fainter magnitudes are reached in these passbands it is useful to look for evidence of intermediate mass, $M > 0.8M_{\odot}$, pre-main-sequence stars in these data. Since the slope of the reddening vector is nearly parallel to the intrinsic color relation in the $V-R$,$R-I$plane, we have not dereddened these stars. Instead Figure 12 is the apparent $V, V-I$ color-magnitude diagram for all the stars in the cluster field separated into 4 annuli of approximately equal area centered on the cluster. A reddening vector of length $\Delta A_v = 0.75$ is shown in the last panel. Two isochrones from the Geneva models (Schaller, et al. 1992; Bernasconi 1996) corresponding to cluster ages of 5 and 10 Myr are overplotted after adjusting them to the cluster's distance $m - M = 11.99$, and a typical reddening, $E_{B-V} = 0.24$. One can immediately see that almost all the bright cluster stars are within $3\farcm75$ of the cluster center (panel 12a) and that there is not a distinct pre-main-sequence at fainter magnitudes in any of the annular regions.

4.3. Mass Function

Figure 13 shows the initial mass function for the cluster out to the coronal radius of $5\farcm5$ (§3.5). The IMF was constructed by forming histograms of the H-R diagram selected stars (§4.1) inside and outside the cluster boundary. In addition, two histograms corresponding to the stars in each region were computed each with bin widths of $\log_{10}(M/M_{\odot}) = 0.2$ but

with the bin centers shifted with respect to each other by $\log_{10}(M/M_{\odot}) = 0.1$. This method helps improve the counting statistics in the bins while reducing any bias in the apparent shape of the distribution arising from the choice of bin centers. This approach has been adopted by other authors for the same reasons (cf. Forbes (1996)).

All four histograms were corrected for the estimated magnitude and radially dependent undercounts as discussed in §3.4. We show the difference between the inner region consisting of all the cluster stars and interloping field stars and the outer region representing only the field contribution. The difference in the areas of the two regions has been taken into account and the final histogram divided by 2 to compensate for the 2× over sampling. The $\pm 1\sigma$ uncertainty limits are the $\sqrt{N}$ counting uncertainties in each bin of the original uncorrected counts propagated through the subtraction of the field star (outer region) histogram (i.e. $\sigma_{\rm net} = \sqrt{(\sigma_{\rm in}^2 + \sigma_{\rm out}^2)/2}$).

Three distinct mass regimes appear in the diagram marked by inflections in the IMF, one at $\log(M/M_{\odot}) \sim 0.9$ delineating the high mass from the intermediate mass regime and the other at $\log(M/M_{\odot}) \sim 0.4$ where the turnover in the IMF at lower masses begins. For comparison, the mean IMF from Scalo (1998) scaled to yield the same mass as observed in the cluster within the mass range $0.4 \leq \log_{10}(M/M_{\odot}) \leq 0.9$ is shown in Figure 13. This is the only mass range where the cluster IMF agrees reasonably well with the Scalo IMF. Even within this mass range, the cluster IMF is not quite linear being slightly concave downward suggesting a small ($\sim 1\sigma$) deficit of the more massive of the intermediate mass (5–8 $M_{\odot}$) stars. When compared to this typical IMF the cluster has an excess of high mass stars and a large deficit of lower mass stars. The presence of the roll-over at $\sim 2.5\,M_{\odot}$ confirms the observation of the turn-over in the mass function by Herbst & Miller (1982).

The total number of stars within the $5\overset{\rm m}{.}5$ apparent radius of the cluster, after subtracting the estimated background contribution is 282. This is within the uncertainties

of Turner, et al. (1980) who counted 291 ± 9 stars (also after a background subtraction) on photographic material. The total mass contained in those 282 stars is $1272\,M_\odot$ (by integration of the histogram) implying a mean mass of $4.5\,M_\odot$ ($\log_{10}(M/M_\odot) = 0.65$). In Table 5 we compare the stellar mass predicted by the "universal" IMF with that observed in the cluster in the three mass regimes, $8.0 \leq M_\odot \leq 70.0$, $2.5 \leq M_\odot \leq 8.0$, and $0.1 \leq M_\odot \leq 2.5$.

4.4. Mass Segregation

To look for possible mass segregation in this young, 5–10 Myr old cluster, normalized radial profiles for the three mass regimes suggested by the IMF in Fig. 13 are shown in Figure 14. Since the cluster appears spherically symmetric and centrally concentrated, empirical King profiles (King 1962) are appropriate for comparison. As with the determination of the IMF, an estimate of the field contribution has been removed by subtracting the mean surface densities determined outside the apparent edge of the cluster (§ 4.3) for each of the three mass regimes. The undercount correction (§ 3.4, Table 4) was also applied although it is only significant to the lowest mass regime ($M < 2.4 M_\odot$). Provided the solar neighborhood Oört constants (Feast & Whitelock 1997) are approximately the same as those in the vicinity of NGC 3293, the tidal radius, $r_t \approx 15\,\mathrm{pc} = 20'$. This value was fixed and the King profile fit using only the (normalized) surface densities to a radius of $6'$ from the cluster center. Finally, the profiles are normalized in the sense that the area under the profile is unity; the surface density at a given radius is the normalized density multiplied by the total number of stars contributing to that profile.

Mass segregation is clearly evident in Figure 14. The high-mass stars, $M > 8.0\,M_\odot$, are more concentrated towards the cluster's center than are the intermediate mass stars, which in turn are considerably more concentrated than the remaining lower-mass stars,

$M < 2.4\,M_{\odot}$, in the cluster field. Exclusive of the inner most bin, the radial distribution of the lower-mass stars appears nearly uniformly distributed within the cluster.

5. Discussion

The IMF of NGC 3293 contradicts the paradigm of a nearly universal mass function in young open clusters that extends well down the main sequence; there appears to be an almost complete lack of stars with masses less than 2.4 $M_{\odot}$ in NGC 3293. Low mass stars have been found in other comparable young clusters such as Ori OB1 (Hillendbrand & Hartmann (1998)) and NGC 6531 (Forbes (1996)).

The radial plots in several mass regimes discussed above show that the massive stars are more concentrated in the cluster core than are the intermediate mass stars. Since the cluster is young, on the order of a few crossing times at most, little dynamical relaxation is expected. Therefore, the observations presented here support the view that mass segregation occurs *while the cluster is forming.* The bright B stars concentrated in the core of NGC 3293 (Figure 1) most likely formed in the central region of the cluster. There is growing evidence that this is indeed the case in many star forming regions (c.f. Carpenter, et. al (1997), Hillendbrand & Hartmann (1998), Raboud & Mermilliod (1998), Bonnell & Davies (1998)).

The derived IMF for NGC 3293, Fig. 13, when compared to the mean Scalo (1998) IMF, shows a significant excess of massive, $M > 8.0\,M_{\odot}$, stars in addition to the deficiency of stars less massive than $2.4\,M_{\odot}$. It is tempting to think that some of the mass incorporated into the additional upper main-sequence stars came at the expense of the lower mass stars. Table 5 compares the mass in stars within the three mass regimes delineated in Figure 13 with that expected from Scalo's mean IMF.

Bonnell, Bate, & Zinnecker (1998) have explored solutions to the problem of building up stars more massive than $\sim 10\,M_{\odot}$, the point at which radiation pressure from the forming star on dust grains halts accretion. In their model, as gas falls into a dense cluster core and accretes (competitively, Bonnel, et. al (2001)) onto the forming protostars, the *total* energy of the cluster *decreases* and the cluster radius shrinks. In this increasingly denser environment, the probability of encounters between protostars becomes more likely. (Their larger size and the presence of accretion disks implies significantly larger collisional cross-sections relative to main-sequence stars). Massive stars are built up by coagulation with low-mass protostars and cloud fragments. (Allen & Bastien (1995) present a pure coagulation model). On the otherhand, Elmegreen & Krakowski (2001) do not find evidence for environmental influences on the mass distribution of proto-stellar cores in the two star forming regions they examined.

There is at least one other young Galactic cluster with a similar, atypical truncation of its IMF. In a recent study of NGC 6231, Sung, Bessell, & Lee (1998) found a distinct turnover in that clusters IMF at $\log m \sim 0.4 M_{\odot}$, essentially identical to the turnover observed here for NGC 3293. In fact, the IMF for NGC 6231 (their Fig. 10) is quite similar in morphology to that of NGC 3293 (Fig. 13) including the flattening of the IMF for the high mass stars (in this case $\gtrsim 12.5\,M_{\odot}$). Examining the Digital Sky Survey images of both clusters reveals a striking similarity in their physical morphology as well, particularly after taking into consideration the different distances, and therefore apparent angular sizes, of the two clusters. One wonders if there are other clusters with similar morphologies and the same truncated IMF indicating a link between cluster morphology and the star formation history of its members (Clarke, Bonnell, & Hillenbrand 2000).

Within the Carina region of the Galaxy, another cluster, Tr 14, has had its IMF determined by Vazquez, et al. (1996). It also exhibits a peak at 2–4 $M_{\odot}$ and a fall off at

lower masses although this is attributed to incompleteness. (Without further investigation this is the best assumption.) Degioia-Eastwood, et al. (2001) identify PMS stars in the cluster but these are intermediate mass stars and appear to have formed continuously over the last 10 Myr. If a turnover in the cluster IMF is a characteristic of clusters in the Carina Arm region of the Galaxy, then the observation of Zhang, et al. (2001) that energy input from the spiral density wave shock is needed in order to explain the observed turbulence and temperature of the associated molecular clouds, suggests a possible environmental influence on the formation of the clusters. This additional source of cloud energetics may be diminished or absent in the better studied local regions of star formation where low mass stars form in abundance. Further work to explore the possibility is warranted.

We would like to thank the University of Toronto for the use of their now closed Las Campanas telescope. This work has been supported by New York State Center for Advanced Technologies grants and various NSF and NASA programs supporting instrument development.

REFERENCES

Allen, E. J. & Bastien, P. 1995, ApJ, 452, 652

Alonso-Herrero, A., Engelbracht, C. W., Rieke, M. J., Rieke, G. H., & Quillen, A. C. 2001, ApJ, 546, 952

Balona, L.A. 1994, MNRAS, 267, 1060

Bernasconi, P. A. 1996, A&AS, 120, 57

Bertout, C., Basri, G., & Bouvier, J. 1988, ApJ, 330, 350

Bessell, M. S., Castelli, F. & Plez, B. 1998, A&A, 333, 231

Bonnell, I. A. & Davies, M. B. 1998, MNRAS, 295, 691

Bonnell, I. A., Bate, M. R., & Zinnecker, H. 1998, MNRAS, 298, 93

Bonnell, I. A., Bate, M. R., Clarke, C. J., & Pringle, J. E. 2001, MNRAS, 323, 785.

Cardelli, J. A., Clayton, G. C. & Mathis, J. S. 1989, ApJ, 345, 245

Carpenter, J. M., Meyer, M. R., Dougados, C., Strom, S. E., & Hillendbrand, L. A., 1997, AJ, 114, 198

Chlebowski, T. & Garmany, C. D. 1991, ApJ, 368, 241

Clarke, C. J., Bonnell, I. A., & Hillenbrand, L. A. 2000, in Protostars and Planets IV, ed. V. Mannings, A. P. Boss, & S. S. Russell (Tuscon: Univ. Arizona Press), 151

Degioia-Eastwood, K., Throop, H., Walker, G., & Cudworth, K. M. 2001, ApJ, 549, 578

Delgado, A. J., Alfaro, E. J., Moitinho, A., & Franco, J. 1998, AJ, 116, 1801

Elmegreen, B. G. & Krakowski, A. 2001, ApJ, 562, 433

Feast, M. W. 1958, MNRAS, 118, 618

Feast, M. & Whitelock, P. 1997, MNRAS, 291, 683

Feinstein, A. & Marraco, H. 1980, PASP, 92, 266

Forbes, D. 1996, AJ, 112, 1073

Graham, J. A. 1982, PASP, 94, 244

Hazen, M. 1991, AJ, 101, 1

Herbst, W. & Miller, D. P. 1982, AJ, 87, 1478

Hillendbrand, L. A. & Hartmann, L. 1998, ApJ, 492, 540

Humphreys, R. M. & McElroy, D. B. 1984, ApJ, 284, 565

King, I. 1962, AJ, 67, 47

Landolt, A. U. 1992, AJ, 104, 340

Massey, P., Lang, C. C., DeGioia-Eastwood, K., & Garmany, C. C. 1995, ApJ, 438, 188

Menzies, J. W., Marang, F., Laing, J. D., Coulson, I. M., & Engelbrecht, C. A. 1991, MNRAS, 248, 642

Munari, U. & Carraro, G. 1996, A&A, 314, 108

Raboud, D. & Mermilliod, J.-C. 1998, A&A, 333, 1998

Rieke, G. H. & Lebofsky, M. J. 1985, ApJ, 288, 618

Rieke, G. H., Loken, K., Rieke, M. J., & Tamblyn, P. 1993, ApJ, 412, 99

Ruprecht, J. 1966, Trans. IAU, 12B, 348

Scalo, J. M. 1986, Fundamentals of Cosmic Physics, 11, 1

Scalo, J. 1998, in ASP Conf Ser. 124, The Stellar Initial Mass Function, ed. G. Gilmore and D. Howell (San Franscisco: A.S.P.), 201

Schaller, G., Schaerer, D., Meynet, G. & Maeder, A. 1992, A&AS, 96, 269

Siess, L., Dufour, E., & Forestini, M. 2000, A&A, 358, 593

Shobbrook, R. R. 1980, MNRAS, 192, 821

Shobbrook, R. R. 1983, MNRAS, 205, 1215

Sung, H., Bessell, M., & Lee, S.-W. 1998, AJ, 115, 734

Turner, D. G. 1978, AJ, 83, 1081

Turner, D. G., Grieve, G. R., Herbst, W., & Harris, W. E. 1980, AJ, 85, 1193

Vázquez, R. A., Baume, G., Feinstein, A., & Prado, P. 1996, A&AS, 116, 75

Zhang, X., Lee, Y., Bolatto, A., & Stark, A. 2001, ApJ, 553, 274

This manuscript was prepared with the AAS LaTeX macros v5.2.

Fig. 1.— Mosaic of V frames covering the NGC 3293 field. N is up and E is to the left. The circle drawn with a solid line has a radius of $5\farcm5$ and is the coronal radius of the cluster, the inner dashed circle $2'$, and the dotted arc NW of the cluster has a $9'$ radius centered on the cluster. The outer boundary encloses the region containing stars used for analysis.

Fig. 2.— Photometric uncertainties (m.e.) in each of the five filters. Note that the magnitude limit in I is limited by the requirement that the star be also measured in V and R.

Fig. 3.— Comparison between the calibrated UBV CCD measures reported here and the photo-electric photometry of Turner, et al. (1980) for all stars in common.

Fig. 4.— The plane in $(B-V, U-B, R-I)$ space perpendicular to the reddening vector **A** (looking down **A**). The projected intrinsic color relations for main-sequence stars ($\log g = 4.0, 4.5$) from Bessell, Castelli, & Plez (1998) are shown marked with $(B-V)_0$ colors for reference.

Fig. 5.— Comparison between the color excesses, E_{B-V}, determined here and those of Turner, et al. (1980) for stars in common. Filled circles are stars where Turner, et al. (1980) based their E_{B-V}'s on MK spectral types and open circles are stars where their color excesses are based on UBV photometry alone. The mean difference is $0\fm011$ and the dispersion $0\fm045$.

Fig. 6.— Effect of changing the reddening law within the $(B-V), (U-B), (R-I)$ color cube. a) $UBVRI$ data projected onto a plane perpendicular to the reddening vector when the reddening law of Cardelli, Clayton, & Mathis (1989) with $R_V = 3.1$ is applied, b) as before but using the reddening slopes determined by Turner, et al. (1980), c) difference in deduced E_{B-V}'s. d) Result if the anomalous reddening law with $R_V = 5.0$ is employed.

Fig. 7.— Expected uncertainties in E_{B-V}, $\log T_e$ and bolometric correction (B.C.) derived

from the dereddening procedure when the observational uncertainties are $0\overset{\mathrm{m}}{.}01$ or $0\overset{\mathrm{m}}{.}02$ in each magnitude. The ordinate is the standard deviation of the distribution about the expected value for 1000 synthetic observations at each $(B-V)_0$ evaluated and the units are in magnitudes for $\sigma_{E_{B-V}}$ and $\sigma_{\mathrm{B.C.}}$.

Fig. 8.— Recovery of artificial stars added to several deep V frames as a function of magnitude and distance from the cluster center. Corrections to the star counts were derived from these.

Fig. 9.— Radial star counts in annular regions of $1'$ width concentric with the center of NGC 3292. a) Counts in 2 dereddened magnitude ranges are shown along with $\sqrt{N}$ error bars. Stars were counted within the bounded region of figure 1. b) Radial star counts using the Digital Sky Survey edition II R image. centered on NGC 3293. These extend to a radius of $15'$ from the cluster and present a more uniform background than in (a).

Fig. 10.— H-R diagram for stars all stars in the field with $U(BVRI)$ photometry ($\sigma_m \leq 0\overset{\mathrm{m}}{.}07$). Evolutionary models are from Schaller, et al. (1992) and the pre-main-sequence models from Bernasconi (1996). The ZAMS is for a cluster distance modulus of $11\overset{\mathrm{m}}{.}99$. The grey band delimits the region from which potential cluster members are selected. 80% completeness limits for U and B photometry are indicated.

Fig. 11.— The lower main sequence of NGC 3293 as defined by stars within $5'.5$ of the cluster center and with reddenings in the range $0.20 \leq E_{B-V} \leq 0.43$. The grey band is the 10 Myr isochrone for the Geneva evolutionary models (Schaller, et al. 1992) adjusted to the distance modulus $m - M = 11.99 \pm 0.13$ previously determined by Turner, et al. (1980) for the cluster.

Fig. 12.— $V, V-I$ CMD in 4 consecutive annular regions of approximately equal area in the field centered on the cluster. The ZAMS and 2 low-mass PMS isochrones corresponding

to cluster ages of 4.6 and 9.6 Myr are indicated.

Fig. 13.— The IMF of NGC 3293 determined as described in the text, §4.3. Scalo's (1998) mean IMF scaled to the cluster mass in the interval $0.4 \leq \log(M/M_{\odot}) \leq 0.9$ is shown for comparison. Our 80% completeness limit is indicated at $\log(M/M_{\odot}) = -0.1$.

Fig. 14.— King model radial profiles for the 3 mass regimes suggested by the breaks in the IMF of NGC 3293 (see fig. 13). The profiles have been normalized to unit area under the curve.

Table 1. Journal of Observations of NGC 3293

Night	Filters (#frames)	Observer, Notes
March 18/19, 1996	$U(5)$, $B(5)$, $V(5)$, $R(4)$, $I(4)$	RWS
March 19/20, 1996	$B(4)$, $V(6)$, $R(3)$, $I(3)$	RWS, non-photometric
March 25/26, 1996	$U(6)$, $B(5)$, $V(4)$, $R(4)$, $I(4)$	RWS
Feb. 4/5, 1997	$U(3)$, $B(6)$, $V(6)$, $R(5)$, $I(4)$	EPH
Feb. 6/7, 1997	$U(3)$, $B(5)$, $V(4)$, $R(4)$, $I(4)$	EPH
Feb. 7/8, 1997	$U(8)$, $B(8)$, $V(5)$, $R(6)$, $I(6)$	EPH, 2 fields
Feb. 14/15, 1997	$U(3)$, $B(4)$	EPH

Table 2. Photometric transformation coefficients

Filter	k_0	$\langle k_1 \rangle$	k_2	k_3
U (a_i)	2.14141	0.4936	-0.19312	0.03871
B (c_i)	0.48864	0.3148	-0.08463	-0.03125
V (d_i)	-0.00195	0.1648	-0.06910	0.00805
R (e_i)	-0.28996	0.1172	0.06406	0.02493
I (f_i)	-0.15000	0.1739	-0.01625	-0.01851

Table 3. *UBVRI* photometry in NGC 3293

α_{2000}	δ_{2000}	V	σ_V	n_V	B	σ_B	n_B	U	σ_U	n_U	R	σ_R	n_R	I	σ_I	n_I	ID#	GSC#
10 35 56.60	-58 10 10.5	15.153	28	7	16.072	28	8	16.561	43	6	14.563	32	7	13.886	19	6	151	
10 35 56.61	-58 11 31.5	10.130	38	8	10.155	16	6	9.345	17	3	10.153	18	8	10.092	31	9	13	0861300344
10 35 56.62	-58 12 40.8	10.218	50	7	10.253	29	9	9.553	20	10	10.239	15	8	10.149	25	9	132	0861301144
10 35 56.62	-58 16 17.0	14.424	48	7	14.793	40	8	14.953	27	7	14.272	26	8	14.017	24	5	251	
10 35 56.75	-58 13 45.6	19.006	84	2	...	0	0	...	0	0	18.889	70	1	18.330	60	1		
10 35 56.76	-58 13 52.0	19.993	119	1	...	0	0	...	0	0	18.969	88	3	18.254	48	1		
10 35 56.81	-58 10 55.3	15.389	26	6	16.908	26	6	18.016	205	3	14.517	34	6	13.613	14	7	157	
10 35 56.82	-58 9 5.7	18.669	88	3	20.014	134	1	...	0	0	17.727	85	3	16.755	25	4		
10 35 56.82	-58 12 57.9	19.676	95	2	...	0	0	...	0	0	18.963	174	4	17.870	74	4		
10 35 56.87	-58 16 20.6	16.664	27	6	17.587	62	7	...	0	0	16.220	19	6	15.770	18	4	252	
10 35 56.91	-58 8 14.5	17.922	61	5	19.005	83	4	...	0	0	17.226	49	4	16.438	20	4		
10 35 56.93	-58 9 18.0	14.767	22	7	15.362	35	9	15.487	25	9	14.417	33	6	14.021	14	7	137	
10 35 56.93	-58 13 39.4	18.241	70	6	18.420	90	2	...	0	0	17.470	79	6	16.781	31	4		
10 35 56.94	-58 20 35.1	18.764	47	1	...	0	0	...	0	0	17.975	32	1	...	0	0		
10 35 56.95	-58 14 9.3	12.932	33	12	13.099	39	11	12.773	29	8	12.855	29	13	12.694	12	9	88	

Note. — The complete version of this table is available from the authors. This printed edition contains only a sample.

Table 4. Experimental undercount fractions

V	$r < 5'.5$	$r > 5'.5$	$M/M_\odot$	V	$r < 5'.5$	$r > 5'.5$	$M/M_\odot$
14.25	0.97	0.98	2.20	17.75	0.90	0.97	1.35
14.75	0.97	0.97	2.15	18.25	0.89	0.95	1.15
15.25	0.96	0.97	2.10	18.75	0.84	0.94	0.95
15.75	0.96	0.94	2.00	19.25	0.80	0.88	0.75
16.25	0.96	0.97	1.90	19.75	0.63	0.74	0.60
16.75	0.94	0.98	1.70	20.25	0.31	0.39	0.50
17.25	0.94	0.94	1.55				

Table 5. Distribution of Stellar Mass in NGC 3292

	$M > 8.0M_\odot$	$2.4 \leq M/M_\odot \leq 8.0$	$M < 2.4M_\odot$
NGC 3293	590	408	202
Scalo (1998)	415	405	1038
Δ	175	3	−836

attachment to manuscript

Click here to download attachment to manuscript: fig1.eps

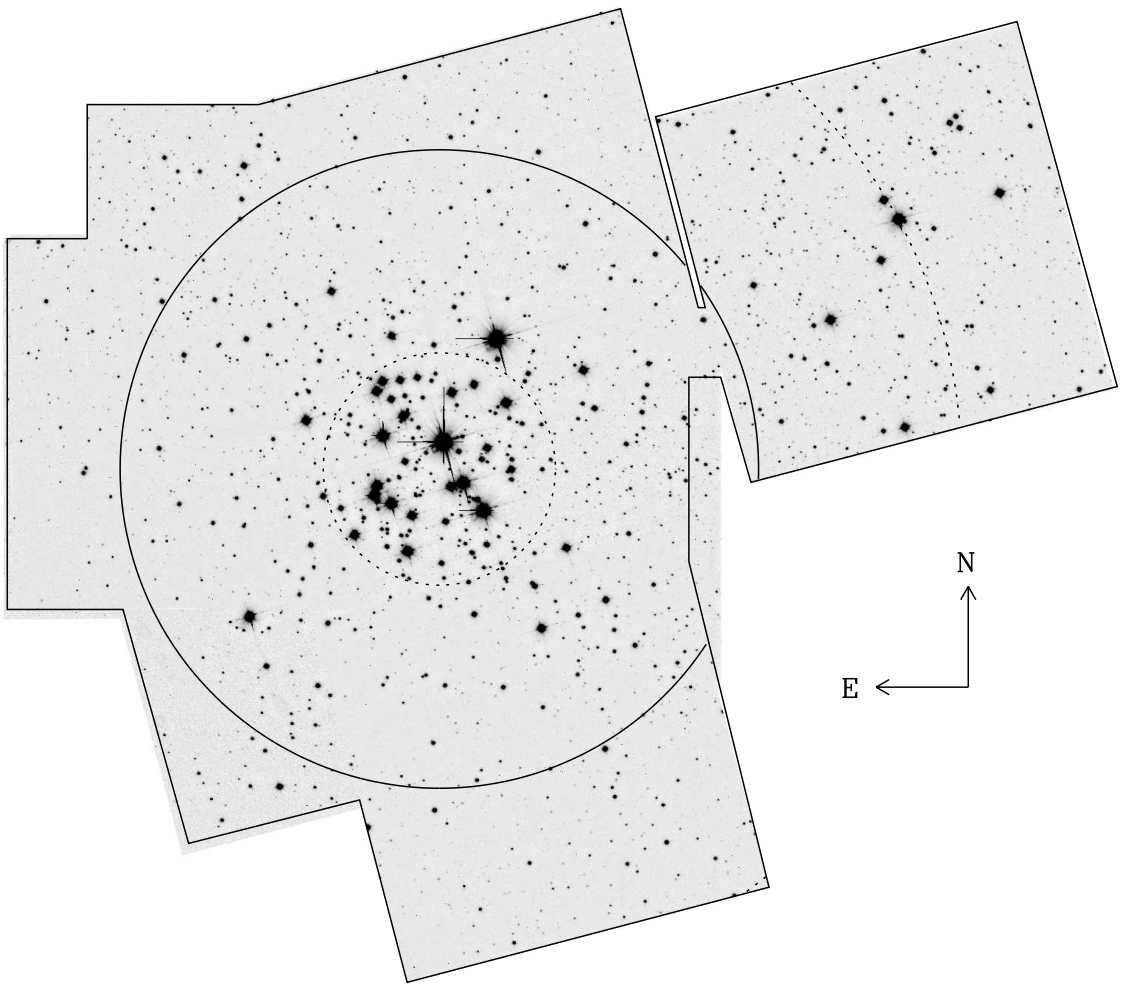

attachment to manuscript

Click here to download attachment to manuscript: fig2.eps

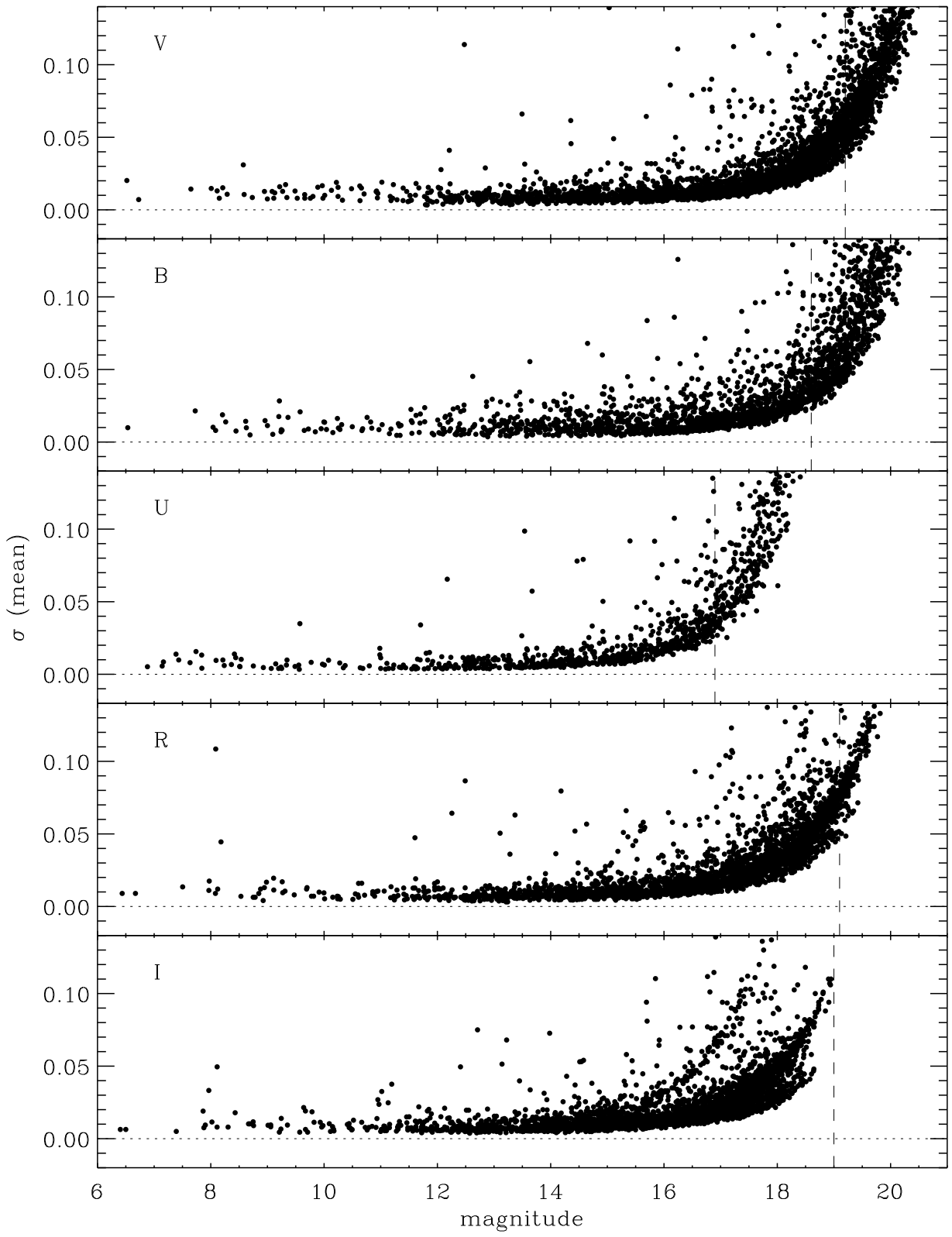

attachment to manuscript

Click here to download attachment to manuscript: fig3.eps

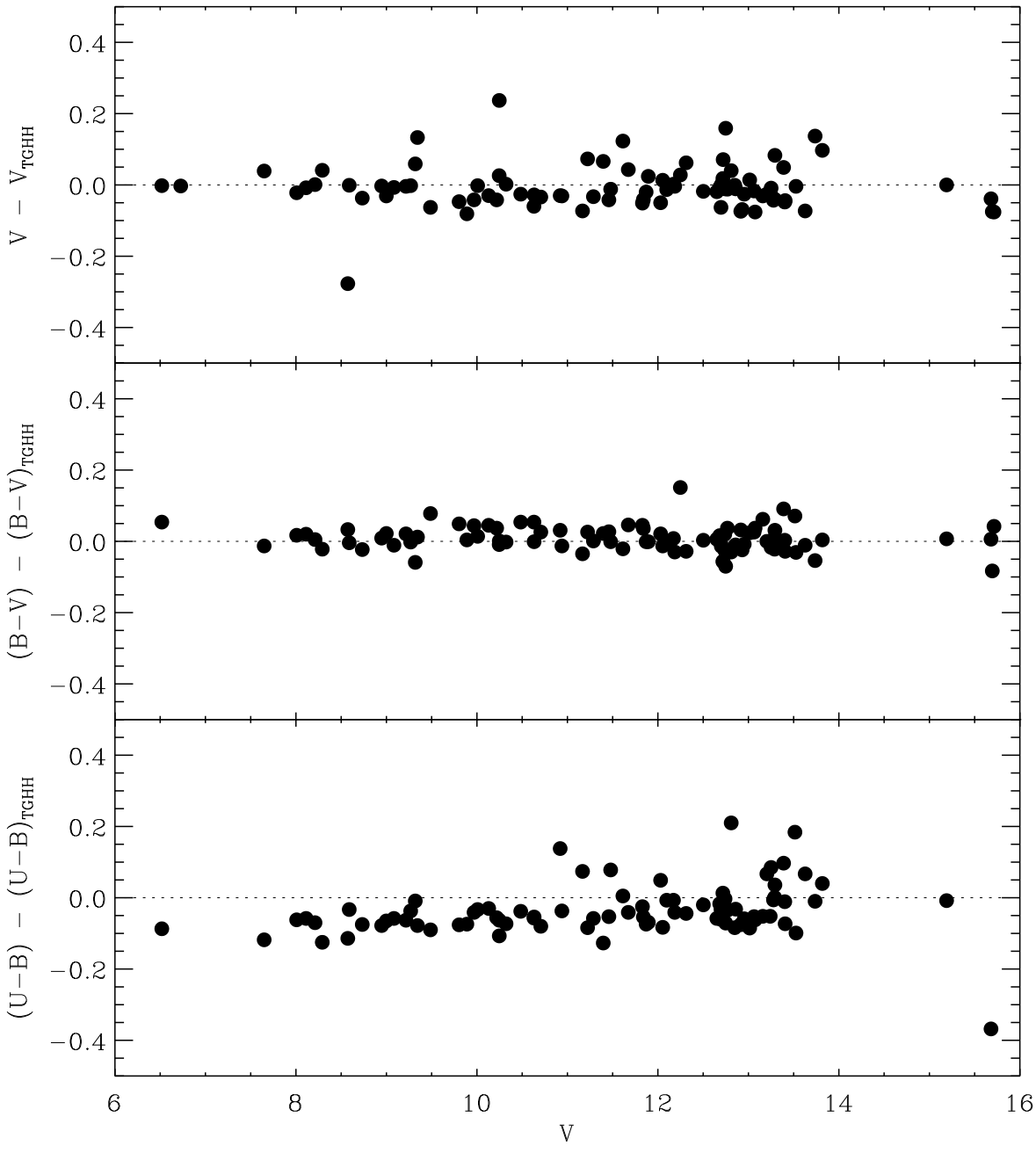

attachment to manuscript

Click here to download attachment to manuscript: fig4.eps

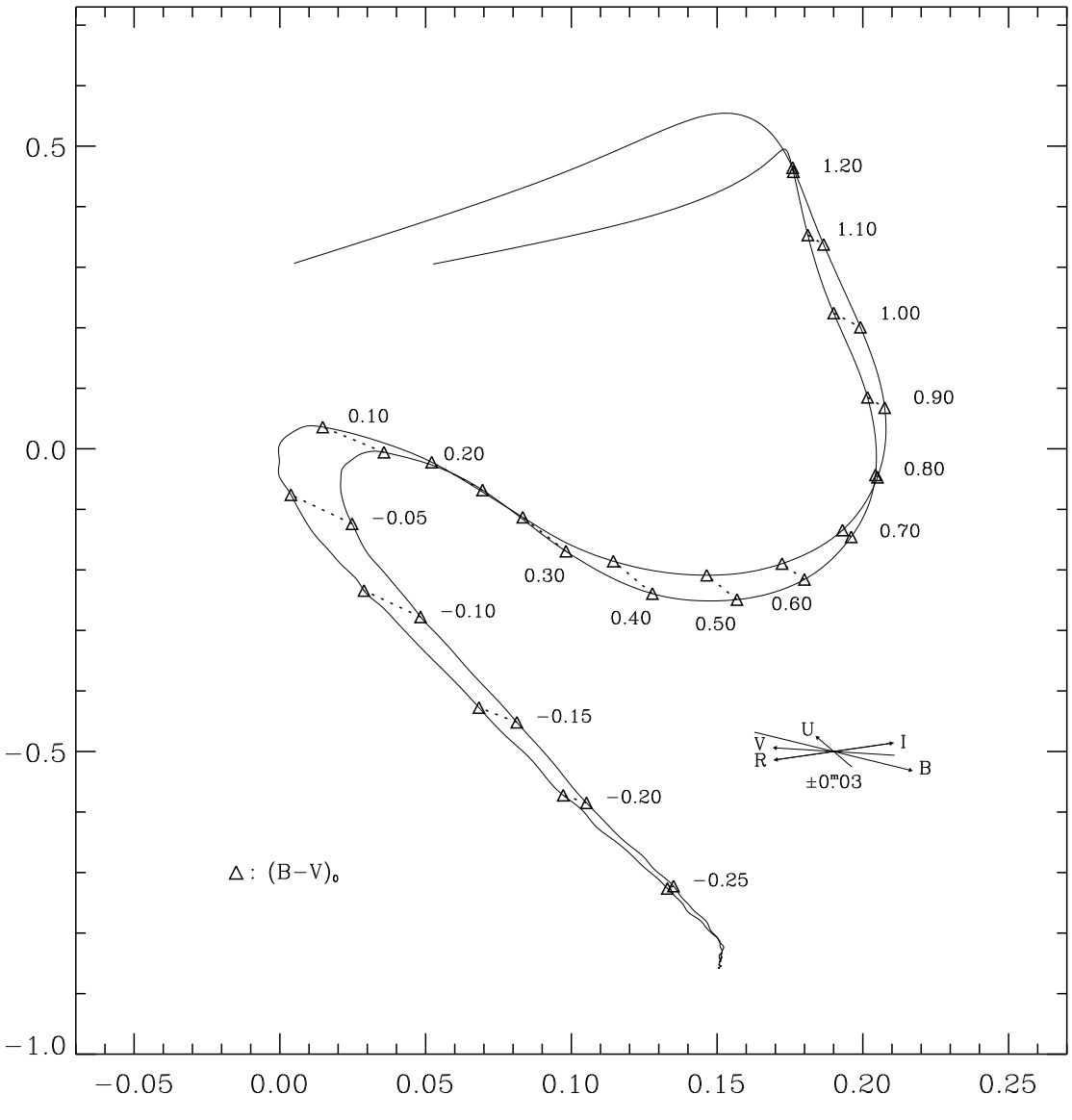

attachment to manuscript

Click here to download attachment to manuscript: fig5.eps

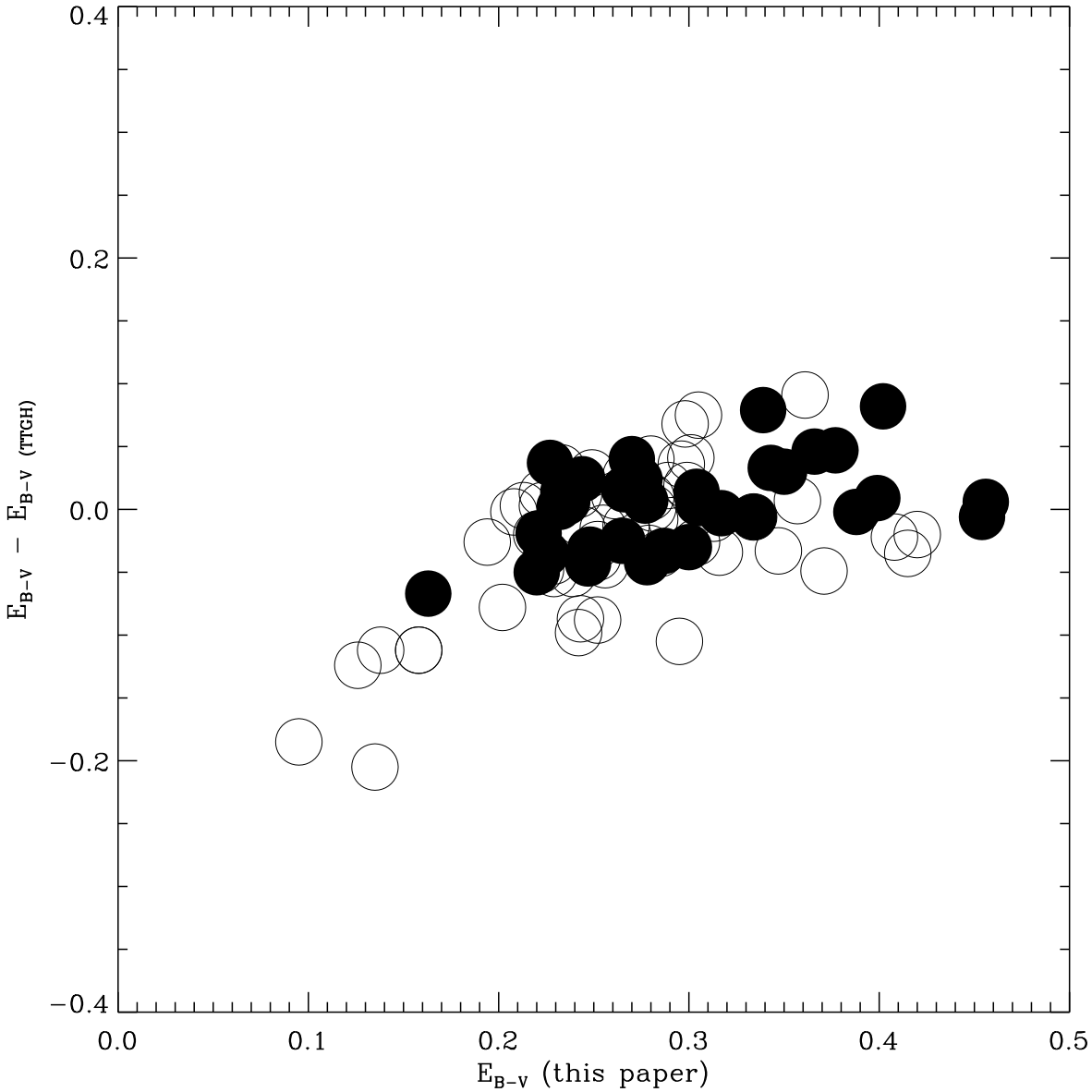

attachment to manuscript

Click here to download attachment to manuscript: fig6.eps

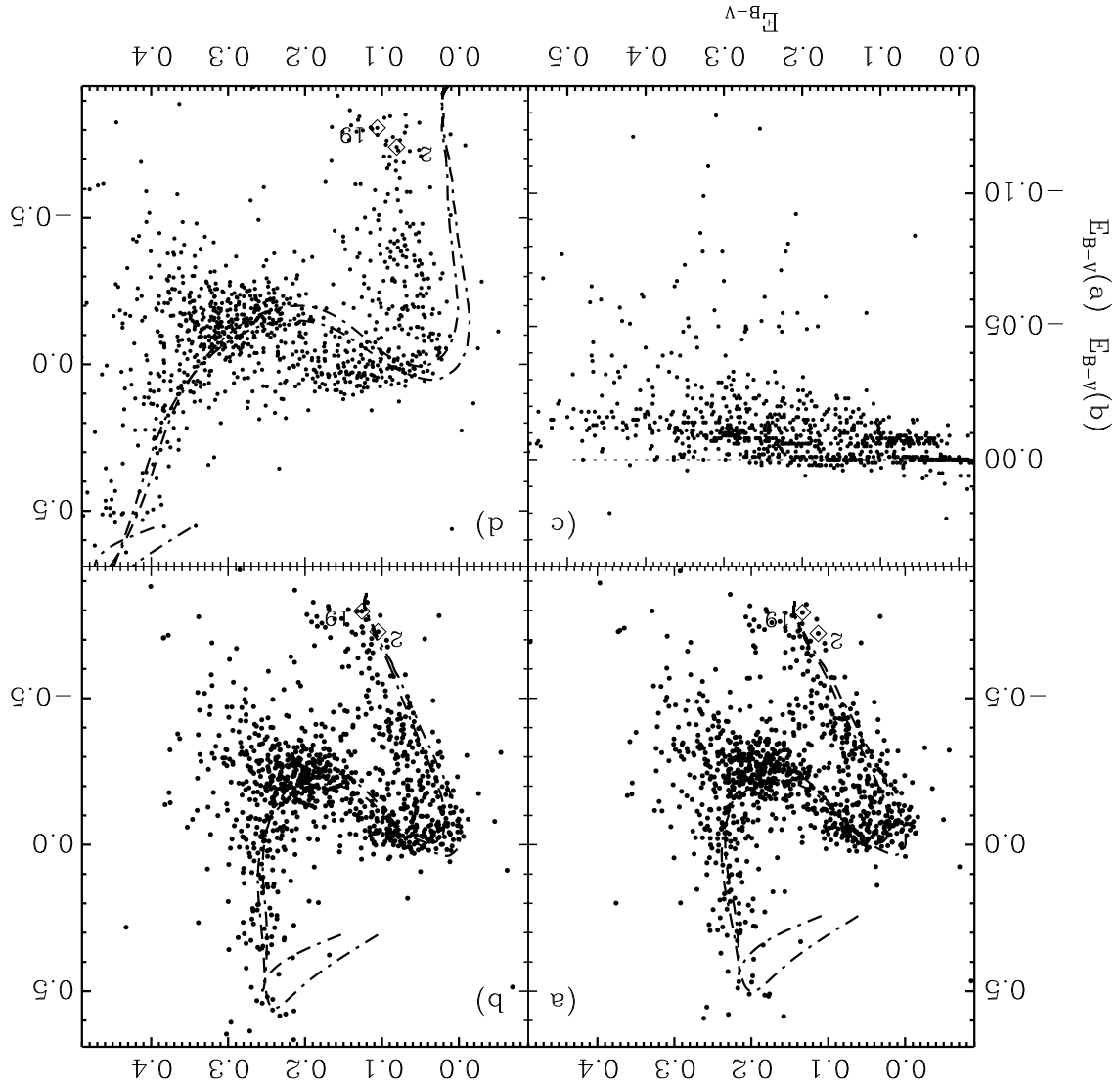

attachment to manuscript

Click here to download attachment to manuscript: fig7.eps

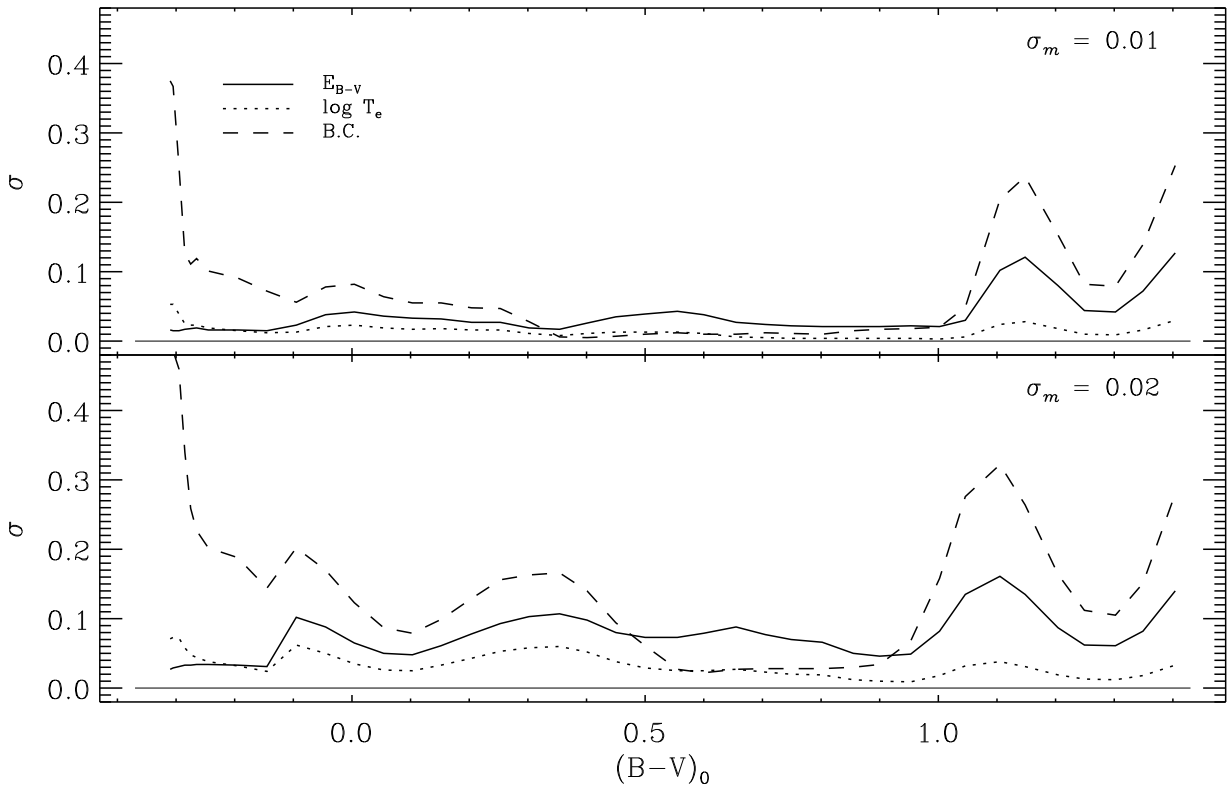

attachment to manuscript

Click here to download attachment to manuscript: fig8.eps

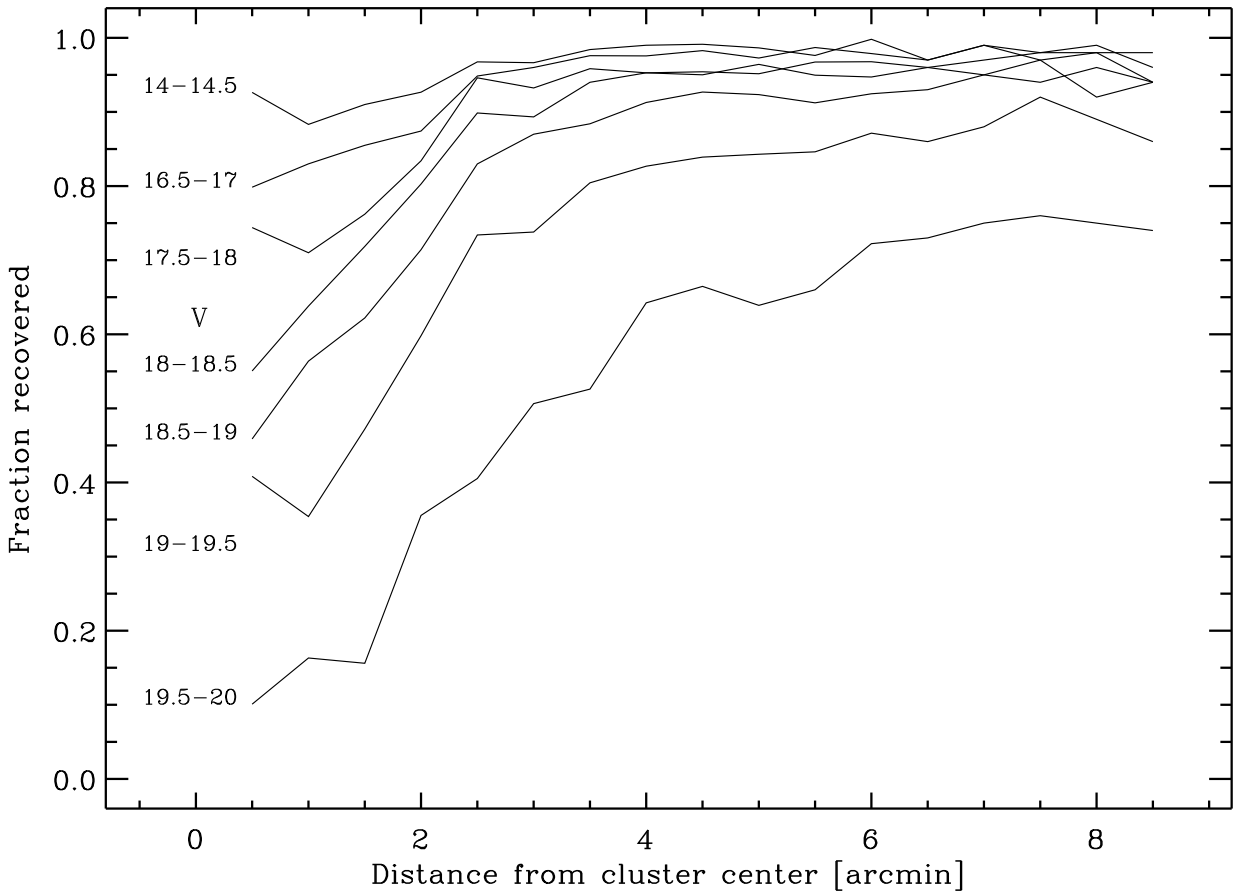

attachment to manuscript

Click here to download attachment to manuscript: fig9a.eps

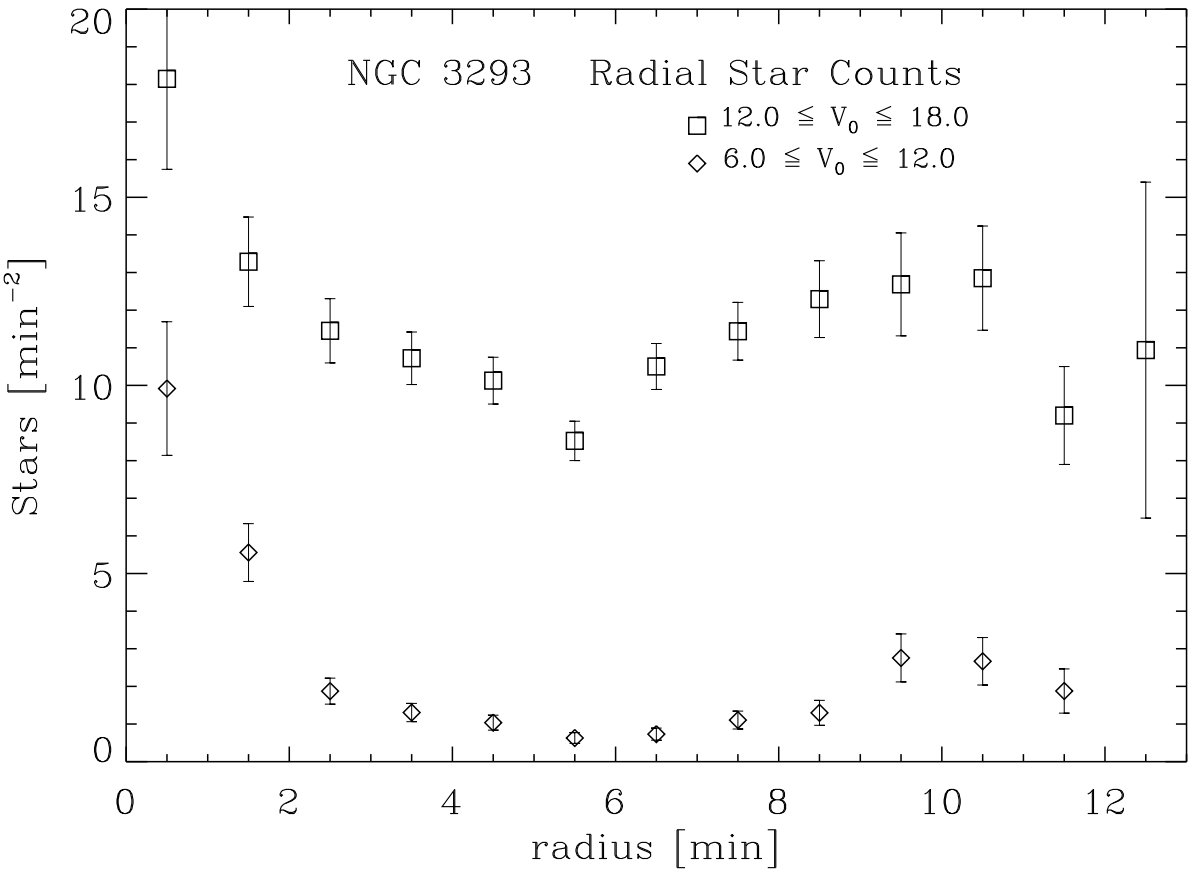

attachment to manuscript

Click here to download attachment to manuscript: fig9b.eps

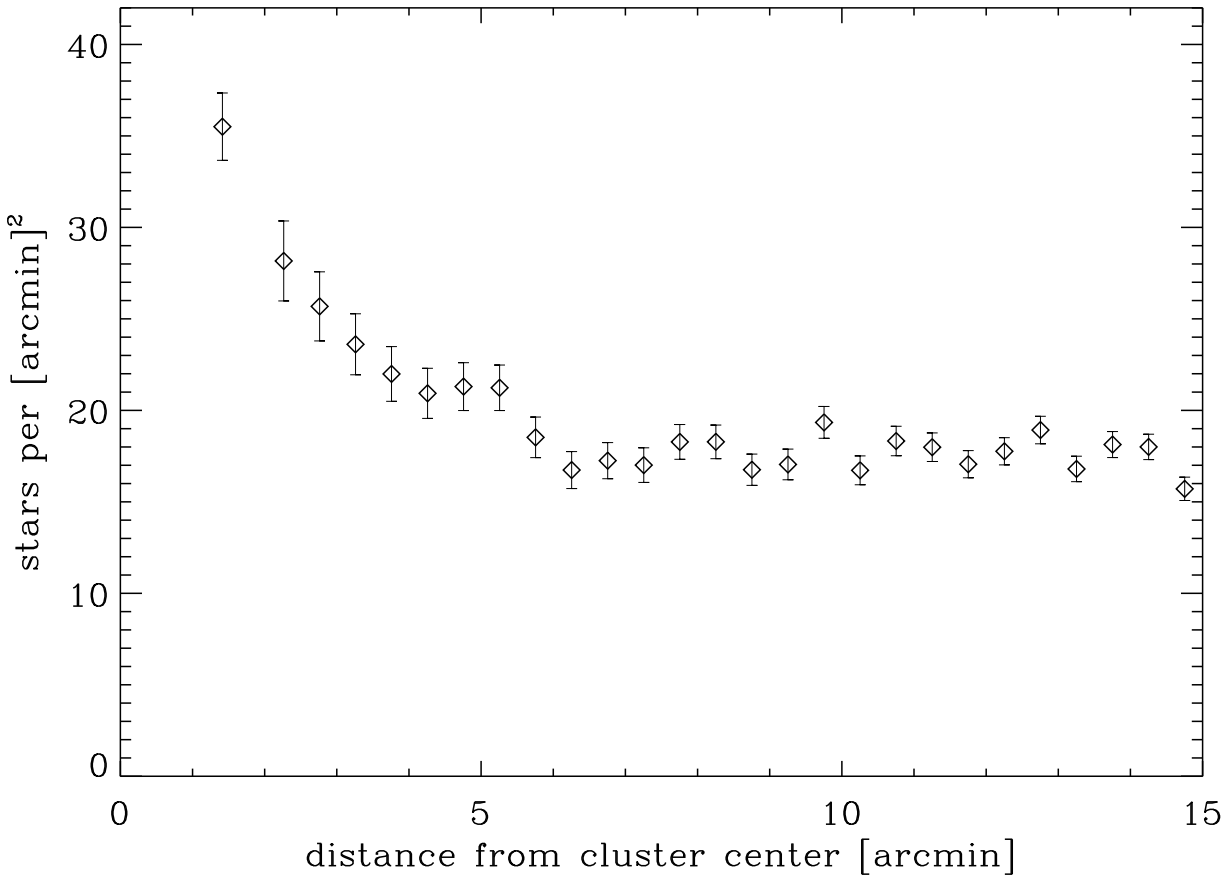

attachment to manuscript

Click here to download attachment to manuscript: fig10.eps

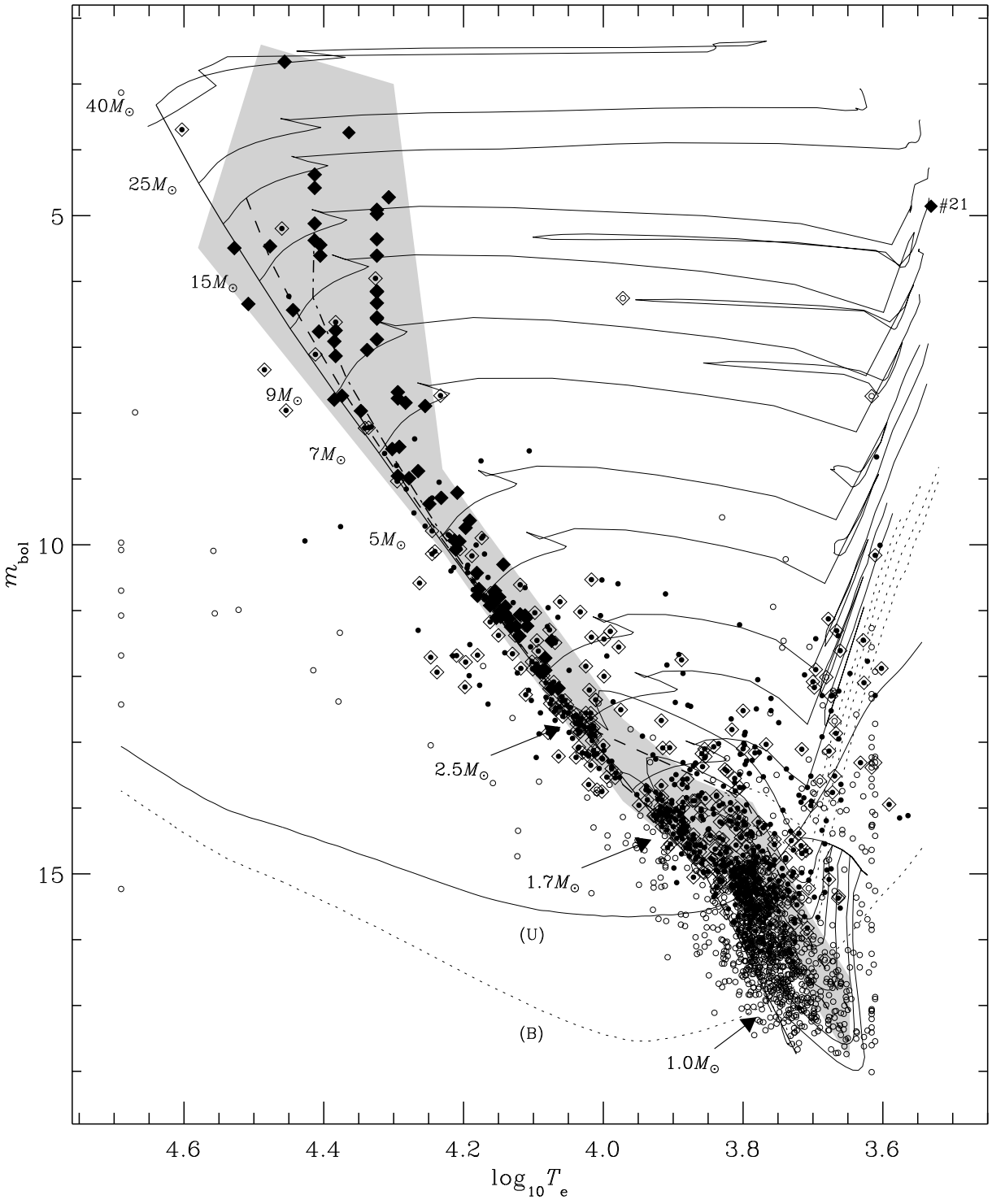

attachment to manuscript

Click here to download attachment to manuscript: fig11.eps

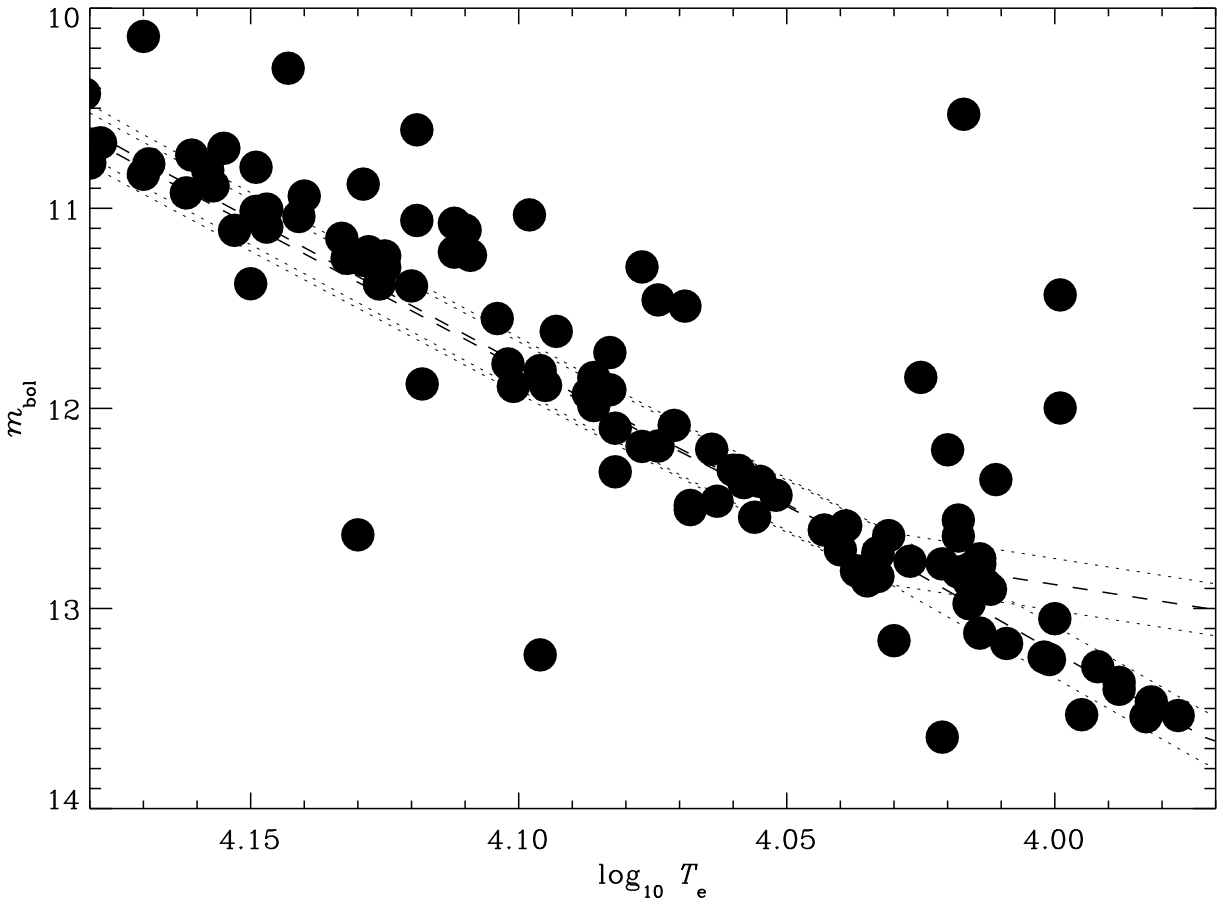

attachment to manuscript

Click here to download attachment to manuscript: fig12.eps

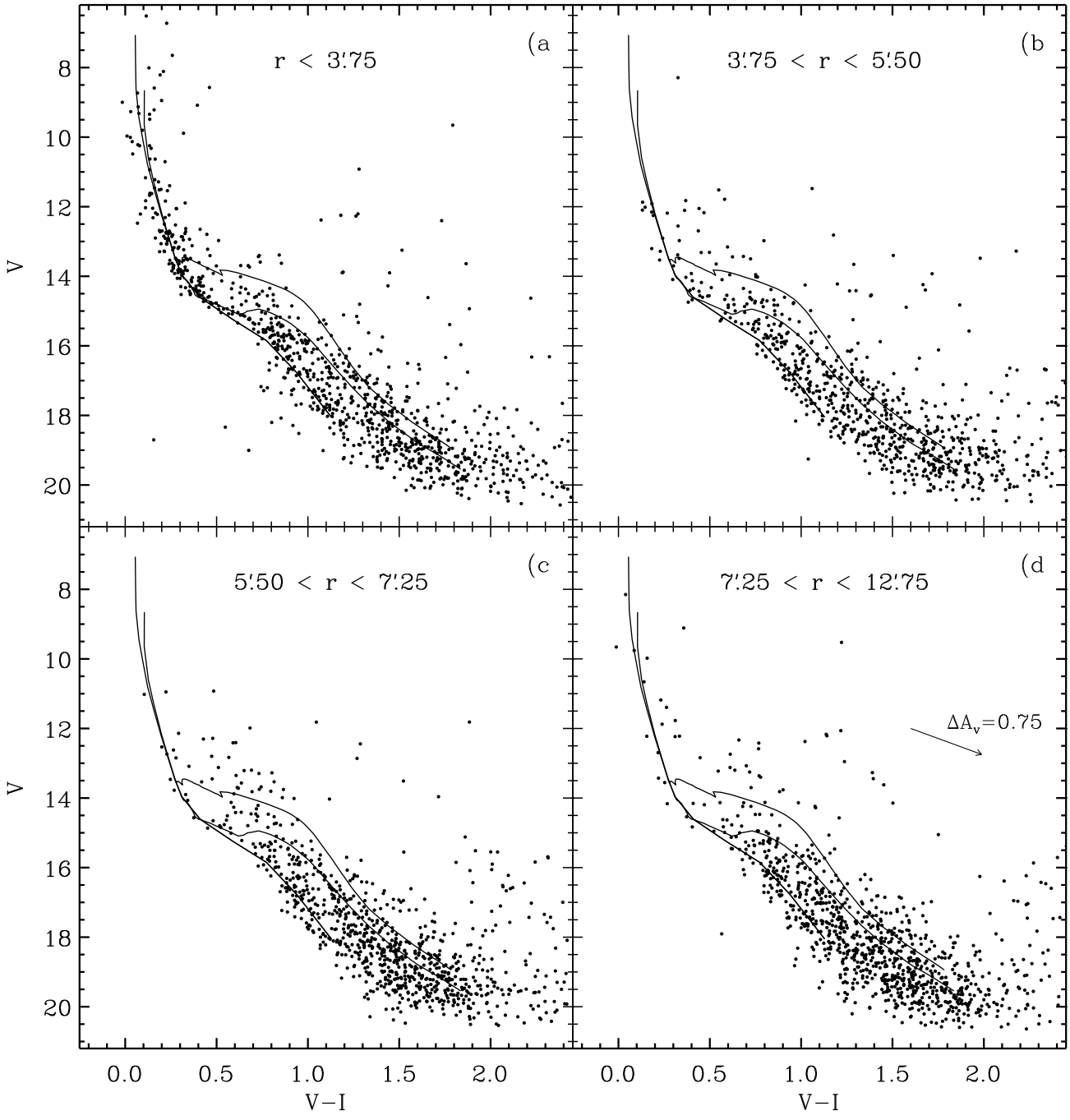

attachment to manuscript

Click here to download attachment to manuscript: fig13.eps

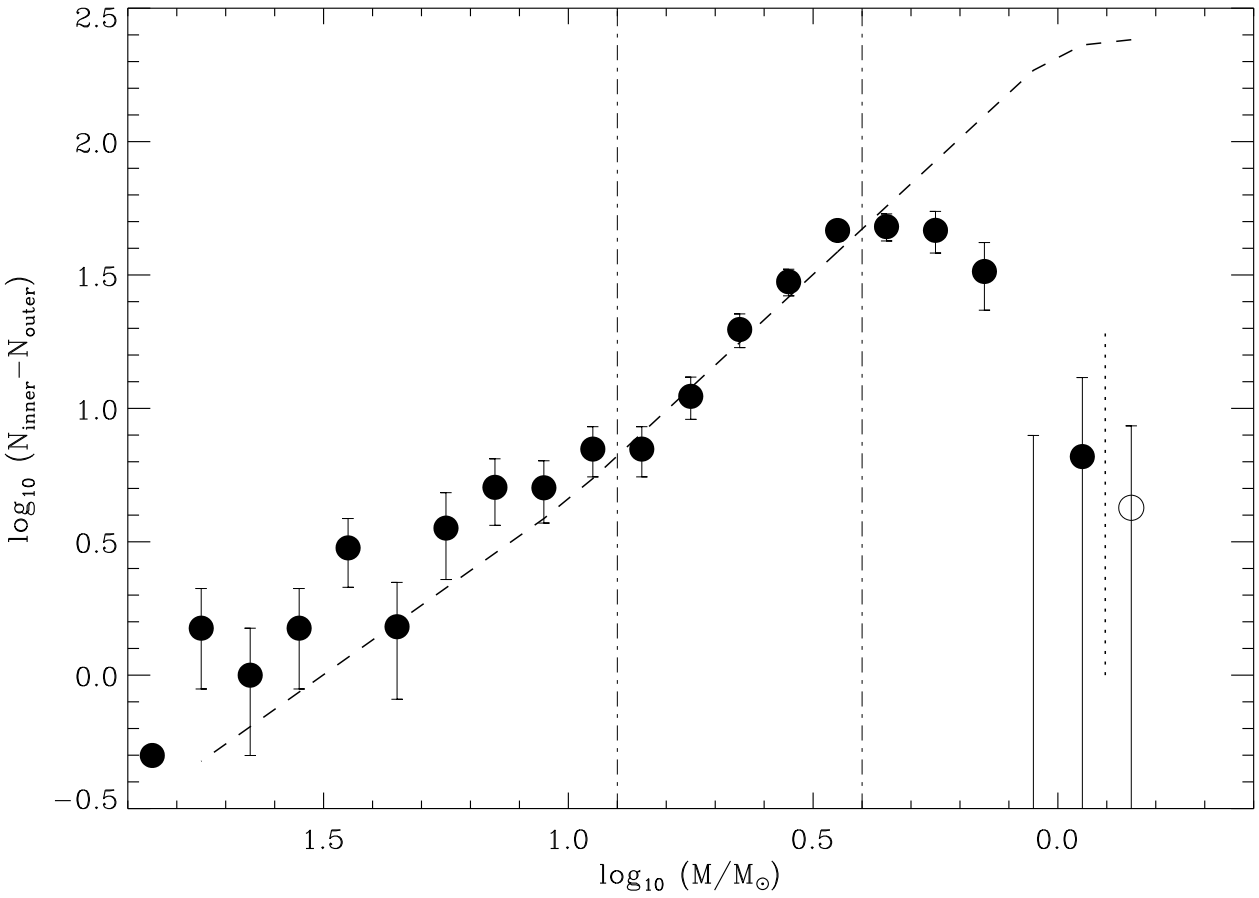

attachment to manuscript

Click here to download attachment to manuscript: fig14.eps